Dayside temperature maps of the upper mesosphere and lower thermosphere of Mars retrieved from MAVEN IUVS observations of O I 297.2 nm emission

J. S. Evans[1], E. Soto[1], S. K. Jain[2], J. Deighan[2], M. H. Stevens[3], M. S. Chaffin[2], D. Y. Lo[4], S. Gupta[2], N. M. Schneider[2], and S. Curry[5]

[1]Computational Physics, Inc., Springfield, Virginia, USA
[2]Laboratory for Atmospheric and Space Physics, University of Colorado, Boulder, CO, USA
[3]Space Sciences Division, U.S. Naval Research Laboratory, Washington, D.C., USA
[4]Climate and Space Sciences and Engineering, University of Michigan, Ann Arbor, MI, USA
[5]Space Sciences Laboratory, University of California Berkeley, 7 Gauss Way, Berkeley, CA 94720, USA

Key Points:

- Our analysis reveals a consistently well-defined mesopause at approximately 120 km.
- We observe an asymmetry in temperatures at dawn and dusk with respect to latitude during different seasons.
- Longitudinal waves with dominant wave-3 component are characterized in both the upper mesosphere and lower thermosphere.

Corresponding author: J.S. Evans, evans@cpi.com

Abstract

We present temperature maps derived from number density retrievals of carbon dioxide (CO_2) for the upper mesosphere and lower thermosphere of Mars using limb observations from the Imaging Ultraviolet Spectrograph (IUVS) aboard NASA's Mars Atmosphere and Volatile EvolutioN (MAVEN) spacecraft. We retrieve CO_2 densities using $O(^1S)$ metastable atoms that radiatively relax by emitting photons at 297.2 nm producing a double-peaked emission profile detectable by IUVS. Retrieved CO_2 densities are used to derive altitude profiles of temperature as a function of latitude, longitude, local time, season, dust activity, and solar activity. CO_2 density and temperature profiles retrieved using the O I 297.2 nm emission feature presented herein extend previous IUVS retrievals from $130 - 170$ km down to 80 km. We validate retrieved CO_2 densities and derived temperatures using coincident measurements and corresponding data products produced by MAVEN IUVS, as available. Analysis of this comprehensive data set, which spans Mars years $32 - 36$, shows (1) a consistently well defined mesopause at approximately 120 km, (2) warming at high pressures (typically below ∼100 km) for a variety of geophysical conditions, (3) asymmetry in temperatures at dawn and dusk with respect to latitude during different seasons (warmer temperatures at dawn during northern hemisphere autumn/winter and cooler temperatures at dusk during spring/summer), and (4) longitudinal waves with a dominant wave-3 component in both the upper mesosphere and lower thermosphere, with lower ($80 - 90$ km) and upper ($135 - 145$ km) atmospheric waves about 65° out of phase.

Plain Language Summary

We show the first O I 297.2 nm emission derived temperature profiles extending from 80 to 150 km in the atmosphere of Mars obtained from observations by the Imaging Ultraviolet Spectrograph onboard NASA's MAVEN spacecraft. This new analysis enables us to bridge the gap and improve our understanding of the coupling that occurs between the middle and upper atmospheres of Mars. Our analysis has revealed thermal variability in the Martian atmosphere with respect to latitude, longitude, local time, season, dust activity, and solar activity. As suggested by previous studies, waves generated in the lower atmosphere propagate to the upper atmosphere, coupling the atmospheric layers, and produce fluctuations in density (up to 40% locally) that can affect the background atmospheric temperature, which is a key parameter driving thermal escape of atomic hydrogen. The density and temperature data presented here provide an important but heretofore missing source of information that is needed to directly link weather and waves in the lower atmosphere to perturbations in composition and temperature in the upper atmosphere.

1 Introduction

Past and present remote sensing observations and *in situ* measurements of the Martian atmosphere, augmented by robust multi-dimensional modeling efforts, have demonstrated that loss of atomic oxygen and hydrogen into space has irreversibly depleted Mars' atmospheric water reservoir (Chaffin et al., 2017; Stone et al., 2020). The drivers of thermal escape of hydrogen are primarily space weather, waves and tides, and lower atmosphere dynamics related to dust storms and deep convection. Understanding the loss of water at Mars therefore requires that we establish a direct causal link between Mars' water reservoir, lower atmosphere weather, and vertical transport mechanisms. Quantifying the coupling between the lower, middle, and upper atmospheres of Mars, especially during solar flares, coronal mass ejections (CMEs), and dust storms, requires coordinated observational and modeling efforts. These efforts must account for dynamical, thermal, and compositional effects that originate in the lower atmosphere but are transported vertically resulting in thermal escape. As suggested by Yiğit (2021), if the atomic hydro-

gen flux into the upper atmosphere isn't limited by diffusion in the lower atmosphere, gravity-wave momentum and energy deposition can affect the background atmospheric temperature, which is a key parameter driving thermal escape. Thus, fully characterizing the thermal structure of Mars' atmosphere from the surface to the exosphere is necessary in order to characterize the vertical distribution of water as well as its dissociation products.

Measuring the temperature of an atmosphere can be achieved through *in situ* measurements as well as remote sensing observations. In the former case, temperatures have been derived using the analysis of aerobraking maneuvers (Keating et al., 1998), precise orbit determination (Forbes et al., 2008), and atmospheric drag (Zurek et al., 2017). Remote sensing approaches include stellar occultations (Gröller et al., 2018; Forget et al., 2009) and use of dayglow observations (Stewart et al., 1972; Leblanc et al., 2006; Evans et al., 2015; Stiepen et al., 2015; Jain et al., 2015; Bougher et al., 2017; Aoki et al., 2022). In either case, the techniques employed rely on relating vertical variations of densities to corresponding temperatures through the scale height (i.e. the distance over which the density of an atmospheric gas decreases by $1/e$).

Three methods have been used to derive temperatures from remote sensing observations of dayglow emissions: (1) an exponential fit to the top-side of emission profiles (Stewart et al., 1972; Leblanc et al., 2006; Stiepen et al., 2015; Jain et al., 2015); (2) a Chapman-like function fit covering the full emission profile including the peak (Stewart et al., 1972; Lo et al., 2015; Bougher et al., 2017; Evans et al., 2020; Jain et al., 2021); and (3) hydrostatic integration of measured or retrieved density profiles (Snowden et al., 2013; Stone et al., 2018). For the first method, the exponential fit must be performed where the atmosphere is optically thin (Leblanc et al., 2006), otherwise the derived temperature is biased (González-Galindo et al., 2021). The second and third approaches explicitly account for a departure from optically thin conditions and we focus on these two approaches in this work. To date, none of these methods allow for direct determination of temperature profiles below ∼130 km.

Historically, the temperature of Mars' upper atmosphere has been derived from remote sensing observations of the CO_2^+ UV Doublet (UVD; B $^2\Sigma_u^+ \rightarrow X^2\Pi_g$) and the CO Cameron Bands (a $^3\Pi \rightarrow X^1\Sigma$). These bright dayglow emissions are typically assumed to originate from CO_2 with no significant contributions from other minor constituents. However, the temperatures derived from these two emissions do not usually agree, with temperatures derived from the Cameron bands being biased high due to non-negligible contributions from CO emissions (Leblanc et al., 2006; Stiepen et al., 2015). Furthermore, temperatures derived from these emissions are constrained in altitude to the region near and above the peak of emission, which typically occurs in the range of 120 to 150 km. To avoid potential biases encountered when using UVD and the Cameron bands and to expand the altitude coverage to the upper mesosphere, we herein make a first attempt to derive temperature profiles using the O(^{1}S) metastable state of atomic oxygen, which is produced primarily by dissociation of CO_2.

Ultraviolet emissions from the oxygen O(^{1}S) metastable state provide a valuable remote sensing signature of energy deposition, photochemistry, dynamics, and thermal structure in the Martian atmosphere and ionosphere. Metastable O(^{1}S) atoms radiatively relax by emitting photons at 297.2 nm (and other wavelengths, such as 557.7 nm; Gérard et al., 2020; Aoki et al., 2022). The oxygen 297.2 nm dayglow vertical profile exhibits a double-peaked structure that was previously predicted by theoretical studies (Fox & Dalgarno, 1979; Simon et al., 2009; Huestis et al., 2010; Gronoff et al., 2012; Jain, 2013) but was never observed by any remote sensing mission prior to MAVEN with the use of the Imaging Ultraviolet Spectrograph (IUVS) (Jain et al., 2015; Gkouvelis et al., 2018).

The production of metastable O(^{1}S) atoms in the Martian atmosphere is dominated by photodissociation of CO_2. While the upper emission peak (near 120 km) is produced

by solar extreme ultraviolet (EUV) photons, the lower emission peak (near 85 km) is produced primarily by solar Lyman α photons. Detection of the lower peak was enabled by a multiple linear regression (MLR) algorithm developed specifically for IUVS data that quantifies the contributions to the highly blended Martian dayglow spectrum, including solar scattered light that becomes important in the upper mesosphere around the lower emission peak of oxygen 297.2 nm dayglow (Stevens et al., 2015b).

Observations of the O I 297.2 nm emission extend from ∼80 km in the upper mesosphere to 160 km and above in the thermosphere, making this emission well-suited for retrieving composition, pressure, and temperature characteristics of the upper mesosphere and lower thermosphere of Mars (this is also true of O I 557.7 nm emission that also arises from the O(^{1}S) parent state; Gérard et al., 2020; Aoki et al., 2022). Accurately characterizing this region of the atmosphere provides an important pathway for understanding the coupling between the mesosphere and thermosphere of Mars. We use the Atmospheric Ultraviolet Radiance Integrated Code (AURIC; Strickland et al., 1999) first principles forward model to perform optimal estimation retrievals of CO_2 densities from IUVS O I 297.2 nm emission profiles. We then perform hydrostatic integration of the CO_2 density profiles to obtain temperature profiles from 80 – 150 km. We validate retrieved densities and derived temperatures through comparison with operational data products from MAVEN IUVS as well as predictions from Mars global circulation models (GCMs). We note that the validation presented here, certainly the one using GCM results, is general and not applicable for individual scans. Since we expect random and natural scan-to-scan variability in retrieval results, our validation is focused on observable trends using data that has been averaged in space or time. However, internal consistency of the retrieval algorithm and resulting data has been verified based on parametric sensitivity studies of all retrieval parameters.

One important advance in this work compared to previous studies on the retrieval of constituents in the Martian upper atmosphere by IUVS is that we include observations from the "inbound" and "outbound" segments of the MAVEN orbit on either side of the periapse segment, which increases the number of profiles for analysis by roughly 37% (for scans with SZA $< 85°$ up to November 14, 2021). In this paper, we first discuss IUVS limb scan observations and the associated geographic and temporal coverage. This is followed by a discussion of the forward model and retrieval algorithms used herein. We then present our methodology for retrieving CO_2 density and temperature profiles using the oxygen 297.2 nm emission feature. In the final sections, we present the results of our study and summarize the most significant insights gleaned from our results.

2 Observations

MAVEN's IUVS instrument (McClintock et al., 2015) is designed to provide global-scale measurements of major molecules, atoms, and ions in the Martian atmosphere by utilizing its 11° x 0.06° slit and occultation aperatures at each end. IUVS has the capability to measure the far-UV airglow (110 - 190 nm) at ∼0.6 nm resolution and the mid-UV airglow (180 - 340 nm) at ∼1.2 nm resolution with a vertical resolution of 5 km (McClintock et al., 2015). The 5 km vertical resolution is from MAVEN IUVS Level 1C data products used as input for the retrieval algorithm. We use the MAVEN IUVS Level 1C data as reported and do not bin or otherwise manipulate the data. Details pertaining to IUVS Level 1C vertical resolution, as well as the field of view, and the observing strategy employed for IUVS can also be found in McClintock et al. (2015).

MAVEN's elliptical orbit initially operated with an apoapsis of ∼6500 km and periapsis of ∼150 km during the primary and first two extended portions of the mission (2014-2019). However, an aerobraking campaign from February 11 - April 5, 2019, implemented to improve MAVEN's availability to support relay communications with assets on the planetary surface, dropped the apoapsis to ∼4500 km and periapsis to ∼130

km. In August 2020, MAVEN periapsis was raised to ∼175 km in order to produce a more fuel efficient and stable orbit. While the changes in orbit (and thus altitude) detailed above affect the science supported by the Neutral Gas and Ion Mass Spectrometer (NGIMS; Mahaffy et al., 2015) aboard MAVEN, it has no impact on the IUVS science supported by the present analysis.

MAVEN IUVS has provided over 145,000 limb scan observations as of November 14, 2021 and we analyze a subset here within the given constraints described below. We use 56,330 dayglow scans comprised of both periapse and inbound/outbound limb segments of MAVEN's orbit constrained to solar zenith angles (SZAs) $\leq 85°$ and local solar time (LST) of $6 \leq \text{LST} \leq 18$ hrs made by IUVS during MAVEN orbits $109 - 15185$ (October 18, 2014 to November 14, 2021). We limit our observations to SZA $\leq 85°$ as biases in the retrievals may exist at larger SZA where an assumption of spherical symmetry may not be valid. The addition of inbound and outbound segments, which are largely antipodal to the periapse segment and can provide dayglow measurements when MAVEN periapsis is on the nightside, increases the number of observations available for analysis. These scans are similar to periapse scans (although with half the observing cadence) in terms of binning and have a similar data reduction process (Jain et al., 2020).

IUVS MUV calibration uncertainties are estimated to be ±30%. This systematic uncertainty originates from the initial flight calibration of the IUVS instrument during the cruise phase of the mission. It represents the range in sensitivity derived from a small set of experiments using stellar targets for which reference spectra were provided by the SORCE SOLSTICE instrument. SOLSTICE was ground calibrated using the NIST Synchrotron Ultraviolet Radiation Facility (SURF) and validated its flight calibration using a model comparison with white dwarf stars, as used by the earlier International Ultraviolet Explorer (IUE) mission.

Since the initial cruise calibration, the IUVS instrument team has been able to explain much of the range in the systematic uncertainty as being due to a combination of flatfield variations on the detector and the inclusion of a limited set of observations of Beta Cephei type variable stars in the original analysis. Calibration correction factors of 0.75 and 0.69, which have not been applied to Version 13 of the data that are publicly available and used here, have been estimated for IUVS CO_2^+ UVD and O I 297.2 nm observations, respectively. These correction factors are derived from additional stellar observations taken on-orbit around Mars and sampling across the full length of the airglow slit image on the detector. For additional details on the current status of the MUV channel calibration see the appendix of Connour et al. (2022). A sub-set of the stellar observations described in that appendix were used to derive the correction factors stated above. The correction factors should be considered an improvement upon the previous calibration, and are consistent insofar as they fall at the edge of the original systematic uncertainty range. The correction factors represent an average sensitivity along the length of the airglow slit and do not account for local flatfield variations, which are within ±10%. These flatfield variations are the primary source of systematic uncertainty in the IUVS data used for the present study.

To examine the thermal behavior of the Martian atmosphere we derive temperature profiles using the O I 297.2 nm MUV emission. IUVS observations enable the simultaneous retrieval of the composition, pressure, and temperature characteristics of the lower thermosphere and upper mesosphere. Limb profiles of O I 297.2 nm emission are extracted from calibrated data using an MLR technique (Stevens et al., 2015b). Example MLR fits of all components to IUVS MUV spectra observed during orbit 3000 on April 14, 2016, as well as the residual fits to the O I 297.2 nm feature, are shown in Figure S1 in the Supplemental Material. The limb profiles used in this study correspond to Level 1C Version 13 Revision 1 data.

3 Forward Modeling of O I 297.2 nm Emission

Table 1. Production of O(^{1}S) atoms and key quantities

Process	Reaction	Quantity	Quantum Yield	References
1a	hν + $CO_2 \rightarrow O(^1S)$ + CO	πF_o(EUV); σ_{1a}^{pd}; σ_{1a}^{abs}	QY_{1a}	(Gkouvelis et al., 2018)
1b	hν + $CO_2 \rightarrow O(^1S)$ + CO	$\pi F_o(Ly_\alpha)$; σ_{1b}^{pd}; $\sigma_{1b}^{abs} = 6.54 \times 10^{-20}$ cm^2	$QY_{1b} = 0.075$	(Gkouvelis et al., 2018)
2	e + $CO_2 \rightarrow O(^1S)$ + CO	σ_2		(Shirai et al., 2001)
3	e + CO $\rightarrow O(^1S)$ + C + e	σ_3		(Shirai et al., 2001)
4	e + $O_2 \rightarrow O(^1S)$ + O	σ_4		(LeClair & McConkey, 1993)
5	e + $O(^3P) \rightarrow O(^1S)$ + e	σ_5		(Laher & Gilmore, 1990)
6	e + $O_2^+ \rightarrow O(^1S)$ + O	$\alpha_6 = 1.95 \times 10^{-7}(300/T_e)^{0.7}$ cm^3 s^{-1}	$QY_6 = 0.05$	(Alge et al., 1983; Kella et al., 1997)
7	e + $CO_2^+ \rightarrow O(^1S)$ + CO	$\alpha_7 = 4.2 \times 10^{-7}(300/T_e)^{0.75}$ cm^3 s^{-1}	$QY_7 = 0.05$	(Viggiano et al., 2005)

3.1 Production and Loss of O(^{1}S) Atoms

Following Fox and Dalgarno (1979), Huestis et al. (2010), Jain (2013), Gkouvelis et al. (2018), and other prior studies, we model the production and loss of O(^{1}S) atoms in order to model O I 297.2 nm slant column emission rates observed at Mars. The known processes that produce O(^{1}S) atoms in the Martian upper atmosphere are provided in Table 1. Quantities $QY_{1(a,b),6,7}$ represent the quantum efficiency of processes 1a, 1b, 6, and 7, whereas $\sigma_{1(a,b),2-5}$ represent photodissociation and photoabsorption cross sections of CO_2 and excitation cross sections for electron impact on CO_2, O, CO, and O_2, respectively. The quantities α_6 and α_7 represent dissociative recombination rate coefficients for CO_2^+ and O_2^+, respectively. The volume emission rate (cm^{-3} s^{-1}) of 297.2 nm photons at each altitude is then given by

$$j(z) = P[O(^1S)](z)(A_{297.2}/(A_{tot} + k_{CO_2}[CO_2](z) + k_O[O](z) + k_{CO}[CO](z))) \quad (1)$$

where P[O(^{1}S)] is the total volume production rate of O(^{1}S) atoms (cm^{-3} s^{-1}) and A_{tot} is the sum $A_{297.2}$ + $A_{557.7}$ of the transition probabilities of the $O(^1S) \rightarrow O(^3P)$ and $O(^1S) \rightarrow O(^1D)$ transitions, respectively. For A_{tot} and $A_{297.2}$, we use the values 1.34 s and 0.08 s, respectively, as recommended by Gkouvelis et al. (2018). We adopt quenching coefficients k_{CO_2} = 3.2× 10^{-11} exp(-1323/T) (cm^3 s^{-1}; Gkouvelis et al., 2018), k_{CO} = 7.4× 10^{-14} exp(-957/T) (cm^3 s^{-1}; Capetanakis et al., 1993), and $k_O < 1.2 \times 10^{-14}$ (cm^3 s^{-1}; Krauss & Neumann, 1975; Slanger & Black, 1981).

There are three primary mechanisms for producing oxygen atoms that are excited to the ^{1}S state: photodissociation of CO_2 (process 1), collisional excitation (processes 2-5), and chemical reactions (processes 6 and 7) (Gkouvelis et al., 2018). Fox and Dalgarno (1979) predicted that photodissociation is the dominant source at all altitudes below 250 km. Four fundamental quantities are required to calculate the production rate of oxygen atoms in the ^{1}S state from photodissociation of CO_2: the CO_2 density, the solar EUV flux, the CO_2 absorption cross section, and the quantum efficiency for production of the ^{1}S state (Gkouvelis et al., 2018). Because of the short effective lifetime of the O(^{1}S) state (∼0.8 s), prior studies have calculated steady state O(^{1}S) density profiles assuming photochemical equilibrium. Detailed model calculations predict that the upper emission peak (near 120 km) is produced primarily by photodissociation of CO_2 by solar EUV photons, whereas the lower emission peak (near 85 km) is produced primarily by photodissociation of CO_2 by solar Lyman α photons (see Figure 6 from Gkouvelis et al., 2018).

Solar EUV radiation drives photochemical processes above approximately 100 km, varying with wavelength and time, and are needed to accurately quantify the impact on

the Martian atmosphere. We use the latest publicly available Level 3 solar irradiance data measured by the Extreme Ultraviolet Monitor (EUVM) on board MAVEN from 19 October 2014 to 14 November 2021 (Version 14 Revision 3). The Level 3 product is a daily modeled solar spectrum from $0.5 - 190.5$ nm derived using three calibrated solar irradiance bands measured by EUVM: $0 - 7$ nm, $17 - 22$ nm, and $117 - 125$ nm bands (full width at half maximum; Thiemann et al., 2017). The modeled spectrum has a native spectral resolution of 1 nm and is rebinned onto a finer wavelength grid for use in forward model calculations. This is achieved by allocating the solar flux into bins of 0.05 nm resolution from $1 - 10$ nm and 0.1 nm resolution from $10 - 105$ nm. Our analysis is not sensitive to the rebinning as the total energy flux is conserved in the rebinned spectrum (Evans et al., 2015). The ionizing radiation (Q_{EUV} = integrated solar irradiance < 45 nm) for the time frame considered in our study ranges from approximately 0.5 to 2.0 erg cm^{-2} s^{-1}.

The production of O(^{1}S) atoms from photodissociation of CO_2 by solar EUV photons (process 1a) is given by

$$P_{1a}[O(^1S)](z) = [CO_2](z) \sum_i \sigma_{1a}^{pd}(\lambda_i)\, QY_{1a}(\lambda_i)\, \pi F_o^{EUV}(\lambda_i)\, exp(-\tau_{1a}(\lambda_i, z)/cos\chi) \quad (2)$$

where $[CO_2](z)$ is the CO_2 number density (cm^{-3}) at altitude z (km), $\pi F_o^{EUV}(\lambda_i)$ is the top-of-atmosphere solar binned EUV flux (Watt m^{-2}), $\sigma_{1a}^{pd}(\lambda_i)$ is the photodissociation cross section (cm^2) for wavelength λ_i (nm), $\tau_{1a}(\lambda_i, z)$ is the vertical optical depth (unitless) above altitude z for wavelength λ_i, and χ is the solar zenith angle (deg). For each wavelength λ_i, $\tau_{1a}(\lambda_i, z) = N[CO_2](z)\ \sigma_{1a}^{abs}(\lambda_i)$, where $\sigma_{1a}^{abs}(\lambda_i)$ is the CO_2 absorption cross section and $N[CO_2]$ is the CO_2 column density (cm^{-2}) above altitude z. For the CO_2 absorption cross section, σ_{1a}^{abs}, we use values reported by Venot et al. (2018). The approximate altitude of unit optical depth as a function of wavelength is shown in Figure S2. Similarly, the production of O(^{1}S) atoms from photodissociation of CO_2 by solar Lyman α photons (process 1b) is given by

$$P_{1b}[O(^1S)](z) = [CO_2](z)\ (\sigma_{1b}^{pd}\, QY_{1b}\, \pi F_o^{Ly_\alpha}\, exp(-\tau_{1b}(z)/cos\chi)) \quad (3)$$

where $\pi F_o^{Ly_\alpha}$ is the top-of-atmosphere solar Lyman α flux (Watt m^{-2}), σ_{1b}^{pd} is the CO_2 photodissociation cross section at Lyman α, and $\tau_{1b}(z) = N[CO_2](z)\ \sigma_{1b}^{abs}$ is the vertical optical depth above altitude z for CO_2 absorption at Lyman α. The altitude of unit optical depth for absorption of Lyman α photons is $\sim$85 km.

Calculation of O(^{1}S) production rates for processes $2 - 5$ requires a photoelectron spectrum as a function of altitude and energy and is obtained using

$$P_l[O(^1S)](z) = n_l(z) \int_{W_l}^{E_{max}} \sigma_l(E)\, \phi(z, E)\, dE \quad (4)$$

where $\sigma_l(E)$ is the cross section for producing O(^1S) atoms by electrons at energy E impacting on the species corresponding to process l, and W_l is the corresponding threshold energy. We obtain the energy distribution function of the photoelectrons by solving the Boltzmann equation for electron transport using AURIC. The AURIC model has been developed for the atmospheres of the Earth (Strickland et al., 1999; Bishop & Feldman, 2003; Bishop et al., 2007), Mars, Titan (Stevens et al., 2011; Stevens et al., 2015a), and Pluto (Stefflet al., 2020). A description of the Feautrier method for solving the Boltzmann transport equation is given by Link (1992), whereas application of the AURIC model to the Martian dayglow is described by Evans et al. (2015), Stevens et al. (2015b), and

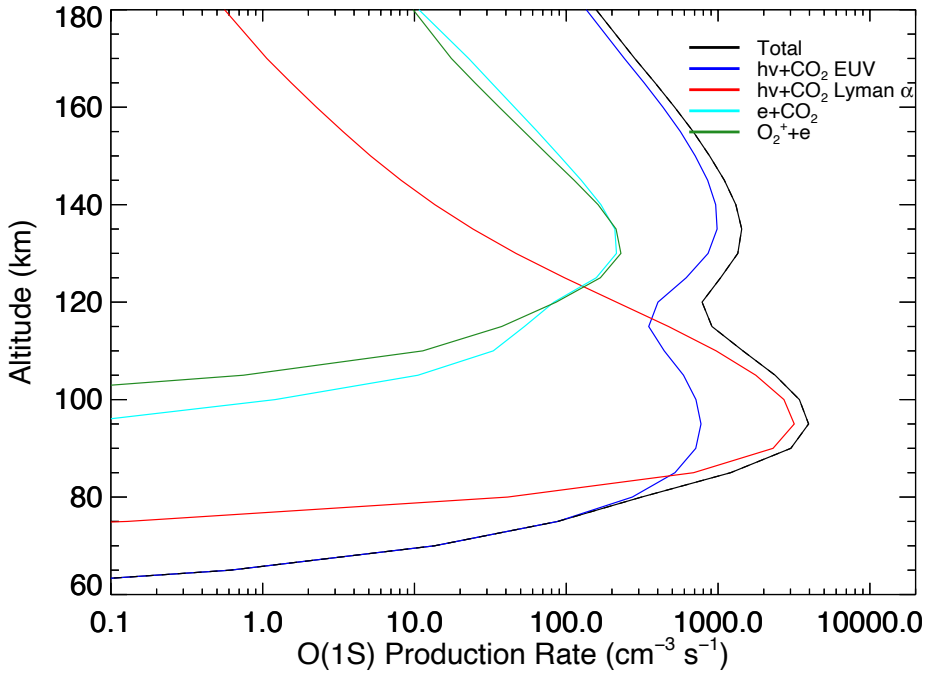

Figure 1. Volume production rate of O(^{1}S) atoms from primary sources for conditions during MAVEN orbit 3000 on April 14, 2016.

Peterson et al. (2016). The sources of excitation cross sections σ_{2-5} for electron impact on CO_2, CO, O_2, and O, respectively, are provided in Table 1.

Following Gkouvelis et al. (2018), we assume that the O_2^+ density is in photochemical equilibrium below 200 km and we use conventional Martian ion chemistry (Fox & Sung, 2001) to calculate its vertical density distribution using photoionization of CO_2 and photoelectron impact ionization of CO_2 calculated with the AURIC model as input to a Kinetic PreProcessor (KPP) photochemical model (Damian et al., 2002). In the conventional Martian ionospheric photochemistry, the main source of O_2^+ ions below 200 km is from the reaction $CO_2^+ + O \rightarrow O_2^+ + CO$. We further assume that the loss of O_2^+ by dissociative recombination equals the production rate from this reaction. That is,

$$P_6[O(^1S)](z) = \alpha_6 \, QY_6 \, [O_2^+](z)^2 \tag{5}$$

where α_6 represents the rate coefficient and QY_6 represents the quantum yield. A similar expression applies for the production of O(^1S) atoms from CO_2^+ + e dissociative recombination. Values for rate coefficients and quantum yields along with their references are provided in Table 1. For low solar activity (Q_{EUV} = 0.5 erg cm^{-2} s^{-1}) and SZA = 0

°

we obtain a peak CO_2^+ density of 2.3 x 10^4 cm^{-3} at 128 km and a peak O_2^+ density of 2.2 x 10^5 cm^{-3} at 122 km, which are in good agreement (within ∼30%) with the model results reported by Fox et al. (2021) for similar conditions using the Fehsenfeld et al. (1970) rate coefficients and O density multiplied by 1.5.

3.2 Description of Forward Model

The AURIC model incorporates a robust time-dependent 1-D (vertical dimension) treatment of Martian photochemistry. Densities of relatively long-lived species are calculated by solving the continuity equation while short-lived species are treated using a photochemical equilibrium approximation. While the robust AURIC photochemical model is appropriate for studying the dominant contributions to O(^{1}S) production and the drivers of its variability, it is computationally intensive and can require up to several minutes of run time on contemporary computing platforms. For our purpose of retrieving CO_2 densities and deriving neutral temperatures from multiple Mars years of airglow measurements, some degree of approximation is required in order to render the problem computationally tractable. Considering the relative magnitude of all the known sources of production of O(^{1}S) atoms in the Martian atmosphere, it is reasonable to exclude processes $3-5$ and 7, since the total contribution from these four processes is estimated to be $\sim$1% (Gkouvelis et al., 2018). Thus, our forward model used for retrieval of CO_2 densities includes the dominant processes, which are 1, 2, and 6 (see Figure 1).

Using AURIC as the forward model for an iterative optimal estimation retrieval algorithm is computationally prohibitive because of the need to calculate photoelectron fluxes required for collisional excitation by electron impact on CO_2 (process 2) and chemical equilibrium O_2^+ densities required for excitation by dissociative recombination (process 6) for each limb scan observation. Thus, we simplify the problem by generating a lookup table containing altitude profiles of O(^{1}S) g-factors (s^{-1}) for process 2 and production rates (cm^{-3} s^{-1}) for process 6 as a function of SZA from 0° to 90° and EUVM Level 3 daily averaged solar EUV irradiance spectra for Q_{EUV} values ranging from 0.5 to 2.0 (erg cm^{-3} s^{-1}). Production rates for process 6 have an additional dependence on CO_2 density, which is achieved by scaling a reference CO_2 density profile by factors ranging from 0.1 to 50 (nine values spaced equally in log base 10). The scale factor is a constant factor applied at all altitudes to the reference CO_2 density profile. The chosen reference atmosphere is the mean over a full Mars year from the Mars Climate Database (MCD) Version 5 (Millour et al., 2018; Forget et al., 1999). The scaling of the reference mean MCD CO_2 density profile is done so that forward model O(^{1}S) production rates for process 6 can be obtained for a wide range of geophysical conditions at Mars. The mean MCD CO_2 profile that we are scaling reflects the mean Mars nonisothermal temperature as a function of altitude. While the exospheric temperature of the reference mean MCD CO_2 density profile is fixed, the density retrievals allow for adjustments in the scale height of CO_2 as required to fit the observed O I 297 nm profiles. The corresponding derived temperatures reflect these adjustments in the scale height of CO_2.

Production rates for specific SZA and Q_{EUV} values are obtained using 2D interpolation of the values contained in the lookup table, with g-factors for process 2 scaled by the retrieved CO_2 density profile for each iteration of the optimal estimation procedure until convergence is achieved. Production rates for process 6 require an additional interpolation over CO_2 density at each altitude for each iteration of the optimal estimation procedure. When constructing the lookup table used by the CO_2 density retrieval algorithm, detailed comparisons were made between the full physics forward model described in the previous section and the approximate forward model described here. These comparisons were performed over the full parameter space of the lookup table to ensure that interpolation over the chosen grid spacing yielded similar results (i.e. within a few percent) between the full physics and approximate forward models.

Simulated O I 297.2 nm limb scan column emission rates (in Rayleighs) for optimal estimation fits to limb scan observations are calculated using

$$4\pi I = 10^{-6} \int_0^\infty j(s) ds \tag{6}$$

where s is slant path distance (km) from the spacecraft along a line of sight and j is the $O(^1S)$ 297.2 nm volume emission rate given by Equation 1. Spacecraft altitudes and limb scan tangent altitudes for each observation are used to define the viewing geometry for calculating simulated O I 297.2 nm column emission rates. Limb scans occurring when the spacecraft is near or within the emitting region (i.e. near or at periapsis) are correctly handled when numerically solving the integral in Equation 6. In the next section, we describe our approach for using the numerical model described in this section for retrieving altitude profiles of CO_2 densities.

4 Retrieval Algorithms

Here we describe the algorithms for retrieving CO_2 density profiles, solar Lyman α flux, and exospheric temperature. The methods for deriving temperature profiles and associated uncertainties are discussed in detail in Appendix A and Appendix B, respectively.

4.1 CO_2 Density and Solar Lyman α Flux

The operational retrieval of CO_2 densities from IUVS dayglow observations heretofore have exclusively used the relatively bright CO_2^+ UVD feature (Evans et al., 2015). The operational profiles, however, have some limitations. Two important limitations are that the vertical sampling of these profiles is relatively coarse (10 km near the peak of emission increasing to 20 km at 150 km) and they only extend down to 130 km. We improve on both of these limitations with the density retrievals described in this section using the oxygen 297.2 nm feature, which allow for a vertical sampling of 5 km (below 170 km) and densities retrieved down to 80 km.

We infer the composition of the atmosphere via IUVS limb scan observations using the Generalized Retrieval and ANalysis Tool (GRANT; Evans et al., 2015; Stevens et al., 2015a), which merges AURIC with OPTimal estimation (OPT; Rodgers, 2000) retrieval algorithms (Lumpe et al., 1997, 2002, 2007) to obtain an optimal atmospheric state solution. The GRANT tool has been applied to dayglow observations of Titan for the retrieval of N_2 and methane (Stevens et al., 2015a) and Mars for the retrieval of CO_2, N_2, and O (Evans et al., 2015; Stevens et al., 2015b). For the present study, we extend the Mars algorithm in order to retrieve CO_2 densities using MAVEN IUVS limb scan observations of O I 297.2 nm emission.

Our forward model calculations assume that the atmosphere is spherically symmetric along the line of sight. This assumption is justified, since for any given tangent height, the emission is produced from within one or two scale heights of the tangent point (roughly $5 - 50$ km, depending on altitude). For tangent heights ranging from approximately 80 to 180 km, the mean extent in latitude, longitude, LST, and SZA are 3.2°, 4.3°, 0.3 hr, and 3.6°, respectively. The maximum extent in latitude, longitude, LST, and SZA (omitting boundary crossing cases that produce large apparent ranges) are 13.0°, 10.4°, 0.7 hr, and 13.0°, respectively. While the typical slant path extent of the four parameters is insignificant, an assumption of spherical symmetry begins to fail for large SZAs because solar azimuth dependence must be considered. Thus, we use 85° as the upper SZA limit for our analysis.

The forward model problem can be expressed in general form as $y = F(x)$ as shown in Evans et al. (2015) with the full forward model F defined by the combination of modeled O I 297.2 nm dayglow and an IUVS instrument model. For density retrievals, the atmospheric state vector, x, consists of 28 parameters: CO_2 density (cm^{-3}) at 26 altitude grid points covering 60 ˘ 600 km, a forward model scale factor that corrects for calibration and model uncertainties associated with the upper peak of O I 297.2 nm emission, and the solar Lyman α flux that drives the lower peak of O I 297.2 nm emission.

While the brightness profiles may extend to much lower and higher altitudes, the signal-to-noise (SNR) ratio drops to ∼5 or less below ∼80 km and above ∼150 km thus resulting in 15 tangent point observations with sufficient SNR. Altitudes outside the 80 − 150 km range are included in the retrieval altitude grid to ensure proper energy conservation in the electron transport code; however, the retrieved CO_2 densities and derived temperatures below ∼80 km and above ∼150 km trend to the *a priori* assumption and are excluded from the data set and our analysis. We explicitly retrieve the absolute solar Lyman α flux so that we can compare the retrieved flux with coincident MAVEN EUVM measurements of this quantity. This comparison provides an important test of the absolute performance of the retrieval algorithm.

The solution to the nonlinear forward model problem is discussed in Evans et al. (2015). The covariance of the solution (see Equation 8 from Evans et al., 2015) is a weighted sum of uncertainties from the *a priori* contribution and direct inversion of the data:

$$\hat{S} = (S_a^{-1} + K^T S_y^{-1} K)^{-1} \tag{7}$$

where S_a and S_y are the *a priori* and data covariance matrices, respectively. The kernel matrix, K, is the derivative of the forward model with respect to the state parameters. The $1-\sigma$ retrieval uncertainties calculated by the algorithm are the diagonal elements of the retrieval covariance matrix $\sigma_i \sim \sqrt{\hat{S}_{ii}}$. The covariance matrix is used in formal error propagation to calculate uncertainties in retrieved densities and derived temperatures (see Appendix B). We note that this approach uses strict formal error propagation and may underestimate the true errors, which must be derived through a detailed error analysis using simulations to quantify individual error components, and is beyond the scope of this study.

The *a priori* covariance matrix S_a characterizes the uncertainty in the *a priori* estimate of the state vector and varies with altitude in the following manner (see Equation 4 from Stevens et al., 2015a):

$$\sigma_{ij}^2 = S_a^{ij} = \begin{cases} [0.25\, x_{a_i}]^2 & i = j \\ \sigma_{ii}\, \sigma_{jj}\, exp[-((z_i - z_j)/(2H))^2] & i \neq j \end{cases} \tag{8}$$

where i and j are altitude indices, z_i is the i^{th} altitude, x_{a_i} is the *a priori* CO_2 density at altitude z_i, $H_i = kT_i/mg_i$ is a length scale (i.e. scale height) that determines the degree of vertical coupling along the rows of the covariance matrix, k is Boltzmann's constant, T_i is the temperature at z_i, m is the molecular mass of CO_2, and g_i is the gravitational acceleration at z_i. Scaling of H_i up or down by 50% changes the retrieved densities at 140 km by less than 20% and and the derived temperatures by less than 20 K for both low and enhanced dust activity indicating that the results are not significantly dependent on the assumed value of H_i.

The diagonal elements in Equation 8 weight the data with altitude in order to facilitate convergence, where the weighting is determined from simulations of the airglow data between 70 and 160 km. The *a priori* CO_2 abundance used to initiate the density retrievals is the mean density as a function of altitude from MCD (Millour et al., 2018) sampled over a full Martian year scaled by the factor $2^{(z_c-115)/7}\times\cos(\mathrm{SZA})$, where z_c is the altitude (km) of the upper peak of the observed O I 297.2 brightness profile determined from a Chapman fit (discussed in the next section). The *a priori* scale factor, which is determined from forward model simulations (discussed below and by Evans et al., 2015), adjusts the *a priori* forward model brightness profile so that the peaks of O I 297.2 nm emission are reasonably close (i.e. within 5 km) in altitude to the observed emission peaks. The reference altitude (115 km) is determined from the upper peak altitude of a model

O I 297.2 nm brightness profile simulated using the *a priori* abundance profile. Increasing or decreasing the reference altitude by 5 km changes the retrieved densities (derived temperatures) at 140 km by less than 10% (10 K) for low dust activity whereas decreasing the reference altitude by 5 km changes the retrieved densities (derived temperatures) by up to 67% (15 K) for enhanced dust activity. This behavior is expected during enhanced dust activity (i.e. higher CO_2 density and peak altitudes), since reducing the reference altitude scales the *a priori* abundance such that the model brightness profile peaks shift substantially in altitude relative to the observed profile causing a significant drop in the convergence rate (i.e. the *a priori* solution requires too many iterations to reach the best fit solution).

The assumed *a priori* temperature profile used to calculate the length scale H_i is the mean temperature from MCD sampled over a full Martian year with an estimated uncertainty of 25%. Inspection of density retrievals applying various *a priori* uncertainties yields an optimal uncertainty value of 25%, which reduces extreme oscillations in the density profile while maintaining goodness of fit of the observed brightness profiles based on Pearson correlation coefficients. We find that varying the assumed *a priori* uncertainty up or down by 50% does not change the retrieved CO_2 densities (derived temperatures) at 140 km by more than 10% (10 K) for low and enhanced dust activity.

We use *a priori* values of 1.0 and 1.8x10^{11} (photons cm^{-3} s^{-1}) for the forward model scale factor and solar Lyman α flux, respectively, each with a corresponding uncertainty of 20%. This *a priori* uncertainty does not represent an uncertainty in the forward model brightness or solar Lyman α flux, but rather allows for flexibility of the retrieval algorithm to control convergence. For the observations with high signal-to-noise used in this study, an increase or reduction of the *a priori* uncertainty by 50% changes the retrieved CO_2 densities (derived temperatures) at 140 km by less than 5% (5 K).

Detailed simulated retrievals spanning the parameter space of the forward model lookup table ($0.5 \leq$ QEUV (erg cm^{-2} s^{-1}) ≤ 2.0; $0 \leq$ SZA (degrees) < 90; $0.2 \leq CO_2$ scale factor (unitless) ≤ 20) were conducted to characterize the performance of the retrieval algorithm. Simulated O I 297 nm brightness profiles were generated using the full physics forward model described in Section 3.1 containing all sources listed in Table 1 to demonstrate that the sources excluded from the approximate forward model used for CO_2 density retrievals do not affect or bias the retrieved densities. For the full parameter space of the simulated retrievals, the mean error of the CO_2 densities for altitudes from 80 to 180 km ranges from a few percent to ~22% in the worst case (SZA = 0°; CO_2 scale factor ~20). The mean error of the retrieved CO_2 density (80 - 180 km) for the full set of simulated retrievals is 7%. The mean error of the retrieved forward model scale factor and Lyman α flux for the full set of simulated retrievals are 1.1% and 1.7%, respectively.

4.2 Neutral Temperature

The methods for deriving altitude profiles of neutral temperature and associated uncertainties are discussed in detail in Appendix A and Appendix B, respectively. In this section we briefly describe the method used to obtain the upper boundary condition required by the neutral temperature retrieval algorithm. We derive exospheric and mesospheric temperatures by fitting two idealized Chapman functions to altitude profiles of O I 297.2 nm column emission observed by MAVEN IUVS as described by Jain et al., 2021, but with the generalized Chapman fitting formalism suggested by Evans et al. (2020). For the MAVEN IUVS data set under consideration here, the problem is generally underdetermined such that the temperature profile tends to be poorly constrained. Thus, our fitting function uses three parameters for each of the two Chapman functions (see Equation 2 in Evans et al., 2020): C, σn_0, and $T(s)$, where gravity varies with altitude, but $T(s) = T$ is a scalar fitting parameter. For the upper peak, we use *a priori* val-

ues of 1, 0.05 (cm^{-1}), and 200 (K) for C, σn_0, and T, respectively. Similarly, we use 1, 0.001 (cm^{-1}), and 150 (K) for the *a priori* values for the lower O I 297.2 nm emission peak. For both sets of *a priori* values, the corresponding *a priori* uncertainties for C, σn_0, and T are assumed to be 100%, 20%, and 100%, respectively. The exospheric temperature (T_0), determined through a Chapman fit to the upper peak of the O I 297.2 nm profile, is utilized as an upper boundary condition for deriving temperatures from retrieved CO_2 densities using hydrostatic integration (see Appendix A and Appendix B). Since T_0 is obtained from fitting the upper peak of the O I 297 nm emission profile, it represents altitudes $\gtrsim$ 140 km. In cases where the Chapman fit fails to converge, a value of 200 K is used for T_0.

5 Methodology

In the following section we describe the outputs obtained by the retrieval algorithm for CO_2 density and temperature obtained via hydrostatic integration of the retrieved CO_2 density. The data are filtered according to the following:

- SZA $\leq 85°$
- Dayside local solar times, $6 \leq$ LST ≤ 18 hrs
- O I 297.2 nm intensity profiles that span from $\leq$ 90 km to $\geq$ 160 km
- Mean of O I 297.2 nm brightness profile $>$ 1 kR
- Two peaks confirmed via Chapman fits of the O I 297.2 nm emission
- Retrieved forward model brightness scale factor ≤ 1.2
- Hydrostatic integration temperatures of $50 - 500$ K for altitudes $\lesssim$ 150 km

The data are binned in pressure and parameter space (latitude, longitude, local solar time, etc.) to create a regular mapping of the data for the creation of the temperature contour maps shown in proceeding figures. The motivation for these constraints and filters is detailed below.

5.1 Density Profile Retrievals

Optimal estimation retrievals of CO_2 densities are obtained from IUVS observed profiles of O I 297.2 nm emission that typically span from 70 to 180 km but may vary from scan to scan. The retrieval algorithm uses 26 altitude grid points with equally spaced increments of 5 km from 60 to 170 km and an exponential grid up to 600 km. We chose a 5 km step size because it corresponds to approximately one scale height (or a fraction thereof) of the Martian thermosphere, depending on altitude and temperature (Stiepen et al., 2015; Bougher et al., 2017; Stone et al., 2018), and is the step size and vertical resolution of IUVS O I 297.2 nm observations (McClintock et al., 2015). For analysis purposes, we only consider retrieved CO_2 densities within the altitude range of the corresponding brightness profile ($\approx 80 - 150$ km).

We retrieve CO_2 density profiles for 51,957 scans with SZA $\leq 85°$ and a convergence rate of 81.4%. Figure 2 illustrates an optimal estimation fit to an IUVS observation of O I 297.2 nm emission on April 14, 2016 at 22:37 UTC during the 9^{th} scan of periapse orbit 3000 (left) as well as the corresponding CO_2 density profile retrieved from the optimal estimation fit to the IUVS observed emission profile (right). The 5 km steps in the altitude profile are the original resolution provided in the IUVS Level 1C data products on the NASA PDS. More details on the vertical resolution and FOV can be found in McClintock et al. (2015). While the errors seem small at 180 km in Figure 2, the emission profiles decrease exponentially above the upper peak (and below the lower peak). As stated previously, we exclude the low SNR regimes at the highest and lowest altitudes. We refer the reader to Figures 2 and 3 from Gkouvelis et al. (2018) for additional examples of IUVS O I 297 nm emission profiles.

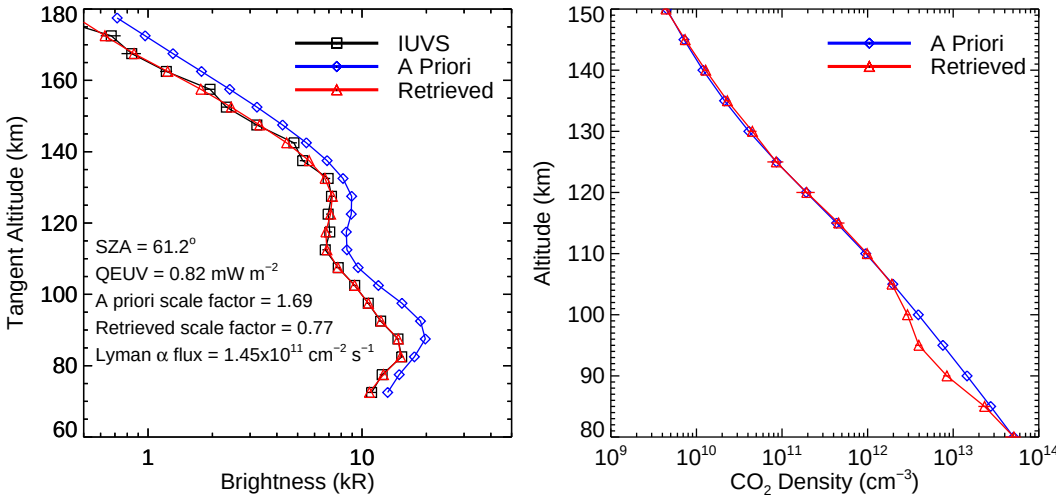

Figure 2. (Left) Optimal estimation model fit (red) to an O I 297.2 nm limb radiance dayglow profile (black) observed by IUVS on April 14, 2016 at 22:37 UTC during the 9^{th} scan of periapse orbit 3000. The blue curve shows the model calculated O I 297.2 nm limb radiance dayglow profile for the conditions of the IUVS observation using an *a priori* mean MCD atmosphere and daily averaged solar EUV irradiance measured by EUVM. The solar zenith angle, QEUV, retrieved scale factor, and retrieved Lyman α flux are shown in the left panel. The black horizontal bars shown with the IUVS data are $1-\sigma$ uncertainties reported in the Level 1C data file. (Right) The CO_2 density profile retrieved from the observed O I 297.2 nm limb radiance dayglow profile is shown in red with horizontal bars showing formally propagated errors. The blue curve shows the *a priori* mean MCD atmosphere used to initiate the optimal estimation fit to the observed O I 297.2 nm dayglow profile.

Figure S3 shows the results of an analysis of the CO_2 retrieval averaging kernel. This matrix describes how the retrieved state vector depends on the true atmospheric state (see Lumpe et al., 2002, 2007, for an extensive discussion). The left panel shows the averaging kernel rows for the ninth scan of orbit 3000. The averaging kernel can be used to quantify *a priori* biases in the retrievals using the relationship $\hat{x} = A\hat{x}_{data} + (I\text{-}A)\hat{x}_{ap}$, where $\hat{x}$ is the retrieval solution vector, A is the averaging kernel, and I is the identity matrix (Rogers, 2000, page 47; Lumpe et al., 2002, 2007). The mean percent contributions from the *a priori* ($\hat{x}_{ap}$) and data ($\hat{x}_{data}$) components of the retrieval solution vector for periapse orbit 3000 are shown in the middle panel. While there is a decrease in the contribution from the data near 120 km (minimum of ~60%), it exceeds the contribution from the *a priori* assumption at all altitudes from 80 to 160 km. The right panel of the figure shows the full-width-half-maximum of the averaging kernel rows, which we use as a measure of the vertical resolution of the retrievals. The vertical resolution varies from ~10 km at 80 km altitude to ~18 km at 150 km, which is sufficient to resolve variations in the CO_2 profile of one or two scale heights.

While the middle panel of Figure S3 indicates that retrieved densities do not exhibit an *a priori* bias between 80 and 160 km (i.e., the data has a greater influence on the retrieval solution than the *a priori* assumption), it is important to also confirm that derived temperatures are not biased by the assumed *a priori* MCD temperature profile. To test for a temperature *a priori* bias we generated two sets of alternative *a priori* CO_2 density and temperature profiles using J. Deighan's one dimensional photochemical model (see Supporting Information for Evans et al., 2022). The first set of *a priori* profiles cor-

respond to a mesospheric temperature of 125 K, a reference CO_2 column density of 10^{20} (cm^{-2}), and exospheric temperatures of 125 K, 150 K, 200 K, 255 K, 300 K, and 350 K. The second set of *a priori* profiles correspond to a mesopsheric temperature of 135 K, a reference CO_2 column density of 2.75 x 10^{20} (cm^{-2}), and the same exospheric temperatures as used for the first set. Figure S4 shows temperature profiles derived from retrieved CO_2 densities using both sets of alternative *a priori* profiles for the eighth scan of orbit 3000 on April 14, 2019 (representative of a quiet dust period) and the eleventh scan of orbit 4072 on November 2, 2016 (representative of an active dust period).

The photochemical model *a priori* temperatures (non-black curves) shown in Figure S4 include cases that are quite different from the MCD *a priori* temperature profile (black curves). In fact, several of the *a priori* profiles are unquestionably nonphysical. However, the temperature profiles derived from the retrieved CO_2 density profiles using the chosen *a priori* predominately fall within 2-σ errors of the values using the MCD *a priori*. The consistency in the shapes of the derived profiles for the selected scans compared to the significant difference in the shapes of the photochemical model *a priori* profiles demonstrates that the derived temperature profiles are effectively independent from the *a priori* below ∼150 km. However, the results of the analysis indicate that derived temperatures may be susceptible to an *a priori* bias above ∼150 km. Therefore, we have constrained the altitude range of the retrieval data set and our analysis to 80 ≤ altitude (km) ≤ 150. Note that the contributions to the solution vector shown in Figure S3 reflect the retrieved densities rather than the temperatures that are derived from the retrieved densities. The derived temperatures are, in fact, more sensitive to the choice of *a priori* density (and temperature) than the retrieved densities, which trend to the *a priori* above 160 km. This behavior is expected given the exponential relationship between density and temperature. The use of 150 km as the upper boundary for our analysis thus reflects the greater sensitivity of the derived temperatures to the *a priori*.

As mentioned in Section 4.1, we independently retrieve the absolute solar Lyman α flux, which drives the lower peak of O I 297.2 nm emission, and compare to daily measurements from EUVM Level 3 data (Figure 3). While the measured solar Lyman α flux is within the standard deviation of retrieved values around solar minimum, there is some variability for scans when the sun is more active. Differences from scan to scan are due to real variations in the atmosphere, or solar illumination (or both), as well as residual solar stray light and other artifacts that are not fully removed in the IUVS Level 1C data processing pipeline. These variations can manifest as variations in the retrieved forward model scale factors or CO_2 densities (or both). The EUVM measurements are typically greater than the retrieved solar Lyman α flux, particularly around perihelion, and we find that this is characterized by a slope of 0.27 when comparing day to day measurements with retrieved values (Figure 3, bottom panel). The behavioral difference and the systematic shift between the measured and retrieved solar Lyman α flux are most likely due to observational effects (i.e. IUVS viewing geometry) and an O I 297.2 nm MUV calibration error discussed in Section 2, respectively. We use these variations in the retrieved forward model scale factors relative to expectations or other independent measurements (e.g., EUVM measured Lyman α flux) as a diagnostic of the technical performance of the retrieval algorithm and resulting data set.

Density retrievals use a forward model brightness scale factor that compensates for systematic biases between the observed brightness and values calculated by AURIC (Picone, 2008). The sources of these biases are primarily from systematic errors in instrument calibration, cross sections used in AURIC, and solar EUV irradiance. IUVS MUV calibration uncertainties are estimated to be ±10%, cross section uncertainties are typically ±25% (Avakyan et al., 1998; Majeed & Strickland, 1997), and EUVM Level 3 daily irradiance uncertainties are ±5% (Thiemann et al., 2017). We find that the retrieved O I 297.2 nm forward model scale factor has a mean value of 0.73 ± 0.09 while the IUVS operationally retrieved CO_2^+ UVD forward model scale factor has a mean value of 0.84 ± 0.09 for pe-

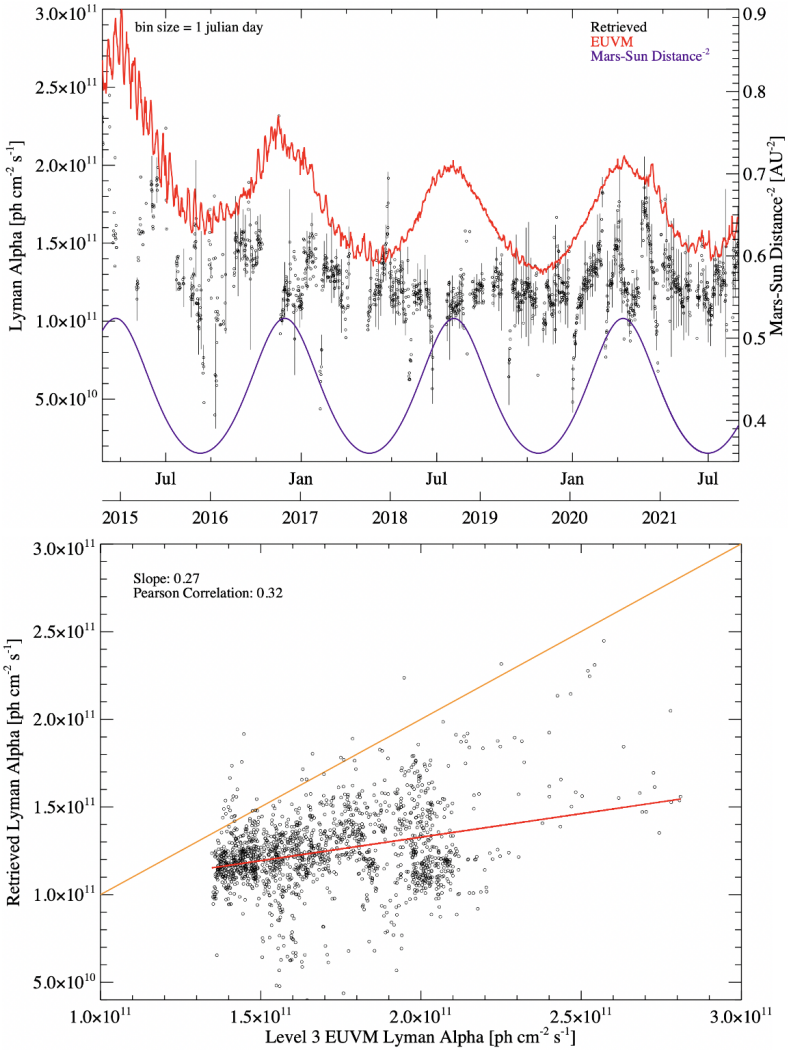

Figure 3. (Top) Model retrieved (black) and EUVM Level 3 (red) Lyman α flux vs Earth month and year. The inverse square of the Mars − Sun distance is shown in purple. (Bottom) Model retrieved vs EUVM Level 3 Lyman α flux. The linear fit is shown in red. The yellow line represents a linear 1:1 relationship. Data are binned in Julian day (bin size = 1 day). EUVM data are daily average Lyman α values from Level 3 Version 14 Revision 3 measurements.

riapse scans. The middle and bottom panels of Figure 4 illustrate the general agreement between retrieved forward model scale factors for both CO_2^+ UVD and O I 297.2 nm periapse retrievals, with a mean difference of -15.7% signifying a shift to slightly lower forward model scale factors from O I 297.2 nm retrievals. For both retrievals, the scale factors of periapse scans typically range from about 0.6 to 1.1 and have distributions within a standard deviation of their respective means. This is similarly demonstrated for inbound and outbound O I 297.2 nm retrievals, which typically have forward scale factors of 0.65 to 1.2 (Figure 4, top panel).

With the IUVS calibration correction factors discussed in Section 2 taken into account, the systematic bias between the forward model and absolute IUVS intensities, evident in Figure 4, will increase. However, this bias does not affect the density retrievals or derived temperatures presented here, since the density retrievals are sensitive to the

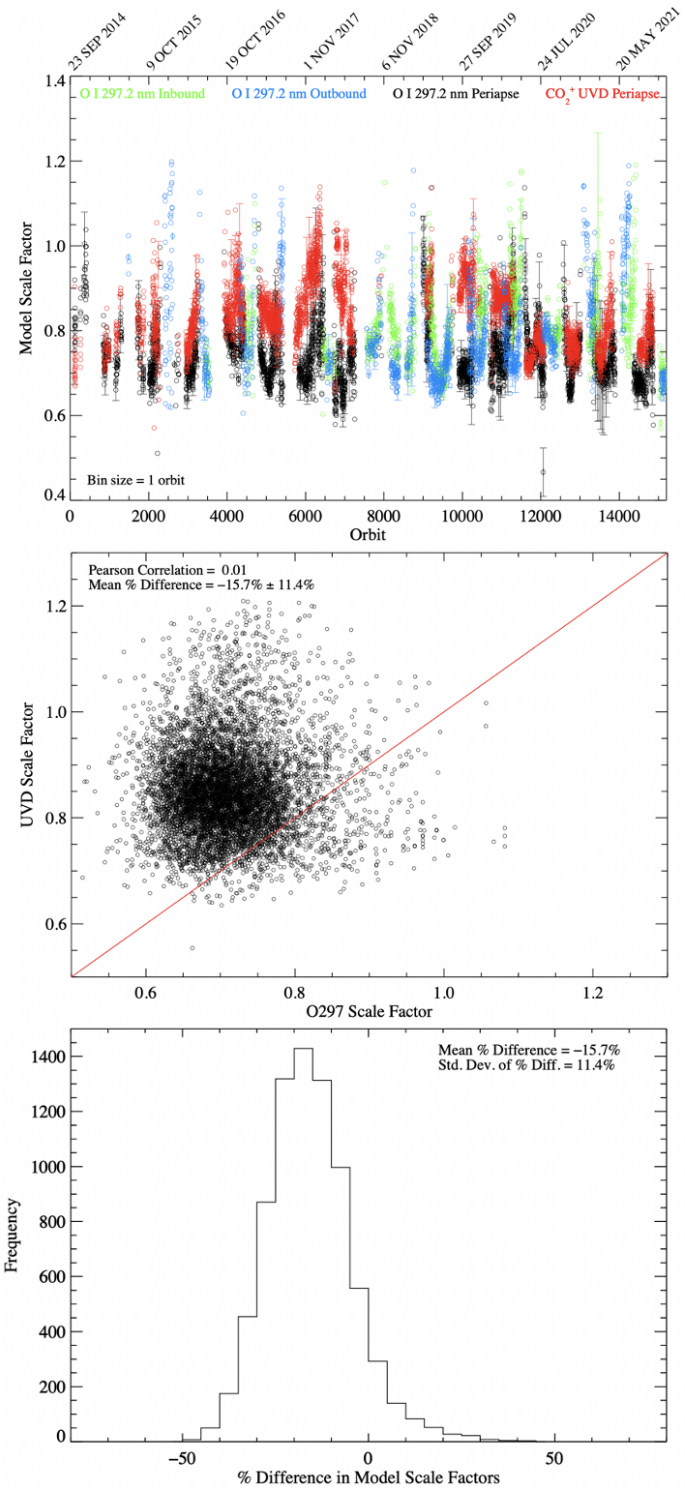

Figure 4. (Top) Retrieved forward model scale factor vs orbit for inbound (green), outbound (blue), and periapse (black) scans retrieved from O I 297.2 nm emission and periapse scans (red) retrieved from CO_2^+ UVD emission. (Middle) Scatter plot of the model scale factors retrieved via CO_2^+ UVD vs O I 297.2 nm emission. Data shown are for periapse scans only. The red line represents a 1:1 ratio. (Bottom) Histogram of the percent difference in the forward model scale factors for periapse limb scans derived from CO_2^+ UVD and O I 297.2 nm emission. The mean percent difference and $1-\sigma$ standard deviation of the percent difference are given for periapse limb scans.

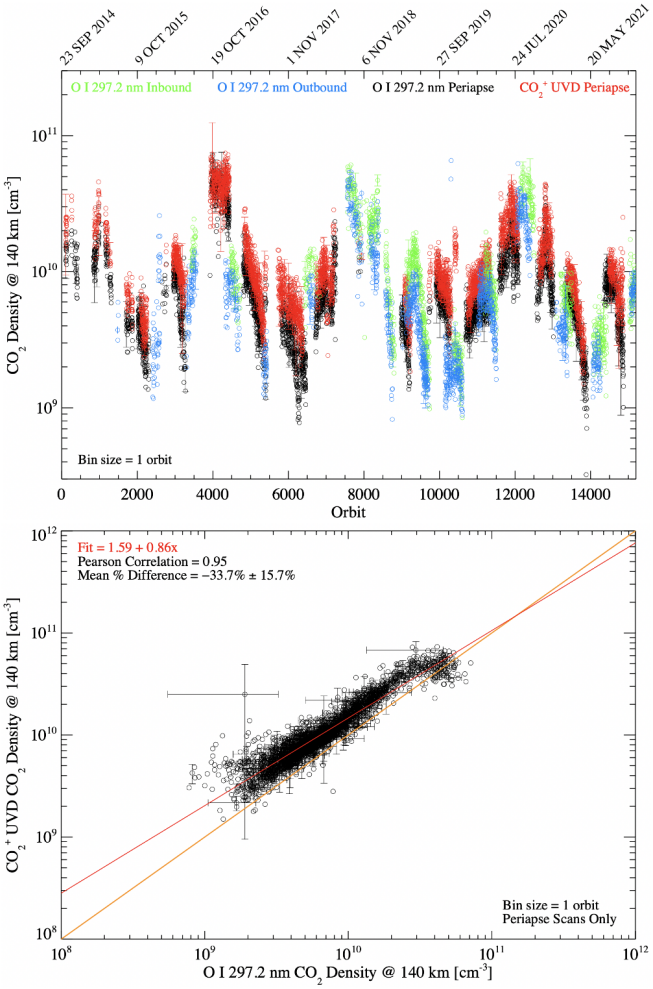

Figure 5. (Top) CO_2 density at 140 km vs orbit for inbound (green), outbound (blue), and periapse (black) scans retrieved from O I 297.2 nm emission and periapse (red) scans retrieved from the IUVS operational data that uses CO_2^+ UVD emission. (Bottom) Scatter plot of CO_2 density at 140 km determined from CO_2^+ UVD and O I 297.2 nm emission. The yellow line represents a linear 1:1 relationship. The red line represents the linear fit to the data in log − log space. The CO_2 densities are binned in orbit and exclude side-segment scans since operational retrievals from CO_2^+ UVD observations for side-segments are currently unavailable.

shape of the observed emission profiles but insensitive to the absolute magnitude (Meier & Picone, 1994; Meier et al., 2015; Evans et al., 2015). In order to mitigate over-fitting and spurious brightness profiles, we remove scans with mean intensity values of less than 1 kR, which are on the very low end for the O I 297.2 nm brightness profile and typically have poorly defined peaks, and forward model scale factors greater than 1.2 (this threshold may change when the data are recalibrated).

In Figure 5 we show CO_2 densities retrieved from IUVS observations of O I 297.2 nm emission at an altitude of 140 km as a function of time (top horizontal axis) and orbit (bottom horizontal axis) compared to operational CO_2 densities retrieved from IUVS observations of CO_2^+ UVD (Evans et al., 2015). Structure in the CO_2 densities is evident most clearly in maxima, which exhibit a strong inverse correlation with the square

of the Mars − Sun distance (Figure 5, top panel). CO_2 densities illustrate a cyclical trend with martian year increasing from roughly 10^9 cm^{-3} in the northern hemisphere spring to over 10^{10} cm^{-3} in the autumn and winter ($L_s > 180°$) similar to trends observed by Aoki et al. (2022) in CO_2 densities derived from O I 557.7 nm dayglow for MY35 to the beginning of MY36. Comparison of densities for periapse limb scans for O I 297.2 nm and CO_2^+ UVD show good agreement over the full range of the mission; however, direct orbit to orbit comparison reveals a systematic shift towards lower CO_2 densities derived from O I 297.2 nm emission characterized by a slope of 0.86 in log-log space (Figure 5, bottom panel). This corresponds to a mean difference in retrieved density at 140 km of -33.7% ± 15.7% for periapse scans. We note that the operational CO_2 retrievals using emission from CO_2^+ evidently saturate in their ability to detect density changes before the retrievals of CO_2 using emission from O I 297.2 nm (Figure 5, bottom panel).

5.2 Neutral Temperature Profile Retrievals

We perform hydrostatic integration of retrieved CO_2 density profiles from 180 to 60 km to derive altitude profiles of temperature and pressure (Snowden et al., 2013; Stone et al., 2018). We use exospheric temperatures retrieved from double Chapman fits to IUVS observed O I 297.2 nm emission profiles as an upper boundary condition for the hydrostatic integration. An example of a double Chapman fit to a MAVEN IUVS limb scan observation of O I 297.2 nm emission is shown in Figure 1 from Jain et al. (2021). Scans that do not have two distinct emission peaks (i.e. the fit fails to identify two distinct peaks or the retrieved parameters are not physically realistic) are excluded from the analysis. In the event an O I 297.2 nm emission profile does not meet the aforementioned criteria or the Chapman fit fails to converge, an upper boundary temperature of 200 K with 20% uncertainty is used for the hydrostatic integration. We note that we derive temperature profiles during each iteration of the optimal estimation procedure since the quenching coefficients discussed in Section 3.1 are temperature dependent. Figure 6 shows examples of temperature profiles, derived from the CO_2 density profiles shown in the figure (blue lines), using the exospheric temperatures (T0) from Chapman fits to the IUVS observed O I 297.2 nm emission profiles as the upper boundary condition. The associated temperature uncertainties, determined by formal error propagation of the density uncertainties (see Appendix B), are also shown.

To analyze gradients in temperature, the temperature profiles are first binned in latitude (bin size = 5°), longitude (bin size = 20°), or local solar time (bin size = 1 hr) and then in pressure with a bin size of $\log_{10}(P) = -0.25$. The data within the corresponding pressure and parameter bin are then used to determine the mean temperatures. In our analysis, we consider viable profiles to be those whose hydrostatic integration temperatures range from 50 to 500 K at altitudes $\lesssim$ 150 km. Therefore, we use 36,053 scans to examine thermal variability where typical temperature uncertainties are approximately ± 17% (60−180 km; ∼16 K (8%) at 140 km). Retrieved CO_2 densities and derived temperatures below the lower altitude limit of the observed O I 297.2 nm brightness profiles are excluded from our analysis.

6 Results

For the first time, CO_2 density and temperature profiles are retrieved using O I 297.2 nm emission in the upper mesosphere and lower thermosphere (80 − 150 km) with results for the higher altitude thermospheric peak consistent with values previously determined with CO_2^+ UVD emission for a narrower altitude range (130 − 170 km) and lower vertical resolution (factor of 2; Evans et al., 2015). We have also added the IUVS inbound and outbound data, which increases the operational database of density and temperature profiles by 37%, typically in places where the periapse observations alone are in darkness and do not provide results. In the results discussed below, temperature map bins

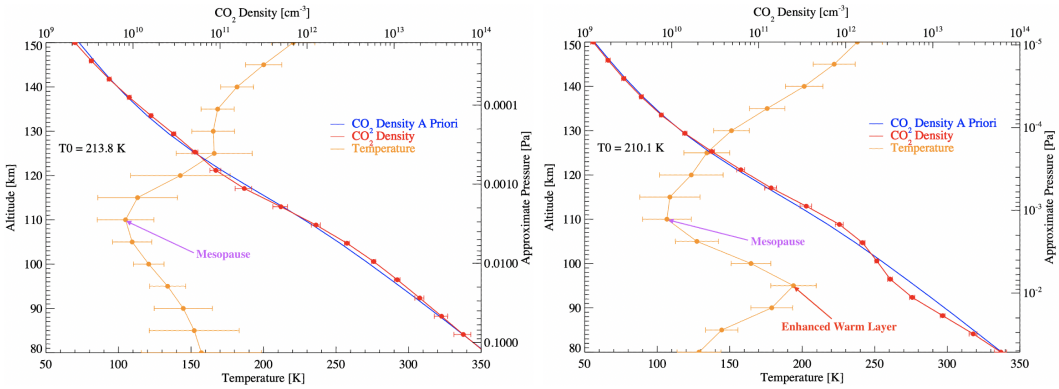

Figure 6. Retrieved CO_2 density (red lines) and derived temperature with corresponding $1-\sigma$ uncertainties (yellow lines) with respect to altitude (and approximate pressure) are shown. (Left) Inbound orbit 3468, 1^{st} scan (11 July 2016 at 00:57 UTC): $L_s = 183.6°$, Lat $= -11.3°$, Lon $= -37.7°$, LST $= 14.4$ hrs, and SZA $= 36.5°$. These profiles are representative of a scan that exhibits no warm layer ($80 - 110$ km). (Right) Periapse orbit 14533, 8^{th} scan (8 August 2021 at 21:38 UTC): $L_s = 82.9°$, Lat $= 58.0°$, Lon $= -104.1°$, LST $= 15.3$ hrs, and SZA $= 48.0°$. These profiles are representative of a region exhibiting a warm layer (indicated by the red arrow) between 80 and 110 km that shows an increase in temperature of over 65 K. The solid blue line is the *a priori* CO_2 density. The upper boundary condition used for hydrostatic integration, T_0, is from the Chapman fit to the upper peak of O I 297.2 nm emission. The mesopause is indicated by the purple arrow.

require a minimum of 50% of the scans within a given latitude/longitude/LST bin to be included in a pressure bin, otherwise that bin is excluded. This applies primarily to the bins at the highest and lowest pressure boundaries. The proceeding figures illustrate results binned in pressure space and constrained in altitude from $80 - 150$ km. Some of the approximate altitudes may extend above and below this range; however, this is due to binning in pressure space rather than altitude space.

Here we present an analysis of 36,053 profiles satisfying the constraints discussed above that exhibit patterns of upper mesosphere warm regions and a mesopause under various seasonal and geographical conditions. The mesopause at approximately 120 km is consistently observed during all seasons. These findings are a direct result of the new approach using O I 297.2 nm emission to extend MAVEN's science output from the lower thermosphere to upper mesosphere for a wide range of conditions thus providing an improved understanding of the coupling between the two regions and the vertical variability and perturbations that drive thermal escape.

6.1 Seasonal and Yearly Temperature Variations

Using temperature profiles determined via hydrostatic integration, we construct thermal contour maps of the full MAVEN mission by Mars season (with respect to the northern hemisphere): spring ($0° < L_s < 90°$), summer ($90° < L_s < 180°$), autumn ($180° < L_s < 270°$), and winter ($270° < L_s < 360°$) (Figure 7). In Figure 7, and all proceeding thermal contour maps, the plots illustrating temperature with respect to latitude (left column, Figure 7) include all longitudes and LST from 6-18 hrs binned in latitude with a bin size of 5°. Likewise plots illustrating temperature with respect to longitude (middle column, Figure 7) include all latitudes and LST from 6-18 hrs binned in longitude with a bin size of 20°, and plots depicting temperature with respect to LST

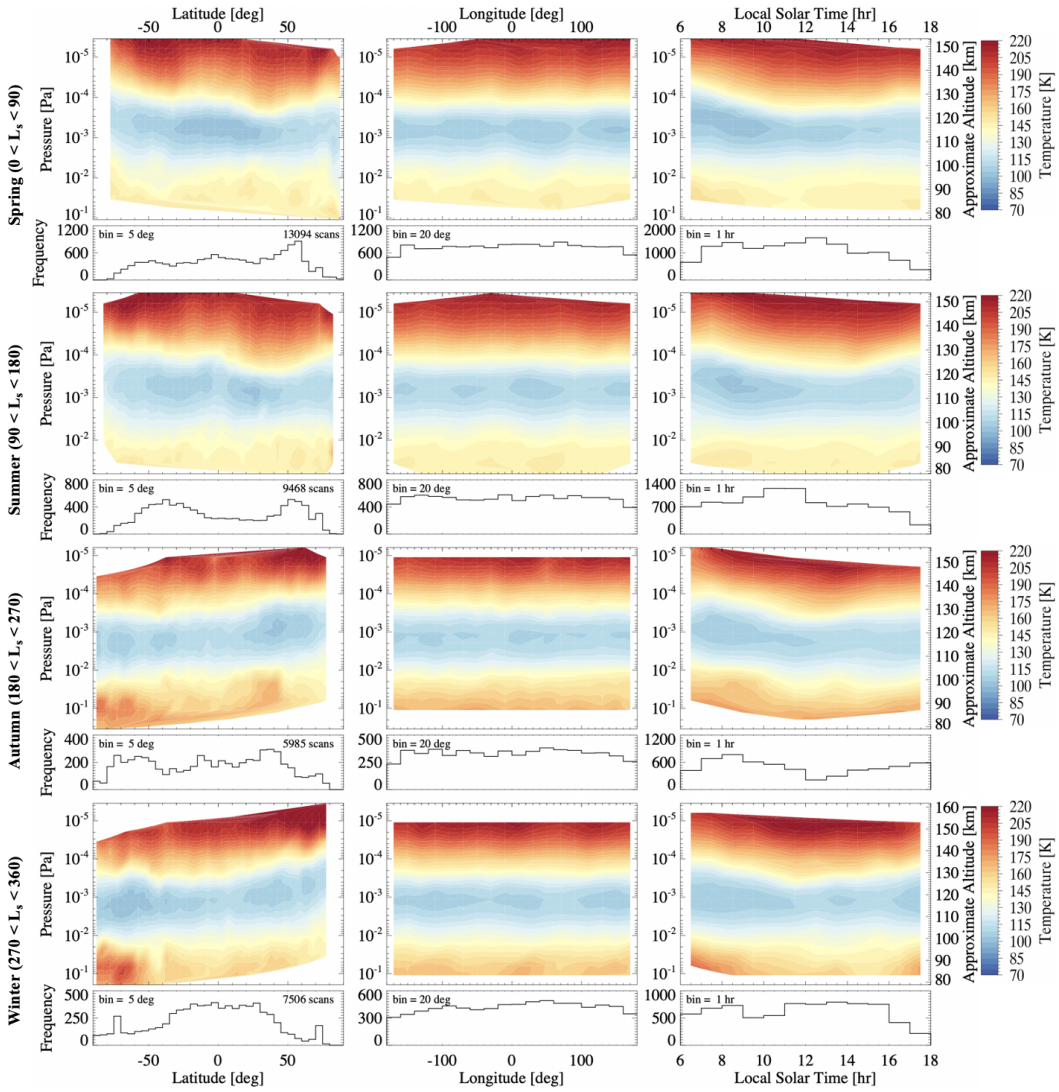

Figure 7. Thermal contour plots for the full MAVEN mission by Mars season. From top to bottom, temperature maps are shown for the spring, summer, fall, and winter northern hemisphere seasons for all latitudes, longitudes, and LST. From left to right, mean temperature contour plots are shown as a function of pressure and approximate altitude vs latitude, longitude, and LST. The corresponding histogram is directly below the contour map. The number of limb scans included in the plots is provided in the upper right corner of the latitude histograms.

(right column, Figure 7) include all latitudes and longitudes binned in LST with a bin size of 1 hr. Each map is comprised of over five thousand profiles with exceptional coverage in latitude, longitude, and LST for all seasons.

We observe similarities in the morphological patterns of the temperature maps shown in Figure 7 across seasons and geographical parameters. Each map exhibits a mesopause at approximately 10^{-3}–10^{-4} Pa ($\sim 105 - 120$ km) in the spring and summer and approximately $10^{-2} - 10^{-4}$ Pa ($\sim 105 - 125$ km) in the autumn and winter, with temperatures decreasing to 100 K or below. (Note that altitudes corresponding to specific pressure levels will vary with conditions and bin size for geophysical parameters.) Plots illustrating binning in longitude, for all latitudes and daytime LSTs, (Figure 7, middle column) show a defined mesopause that spans the full longitude range at approximately 10^{-3} Pa ($\sim$115 km). The frequency of each longitude bin exceeds 200 scans, establishing statistical significance for this feature of the temperature profile. The mesopause is likewise observed in the LST temperature maps (Figure 7, right column) at approximately 10^{-3} Pa, with all LST bins exceeding 150 scans. Warming below the mesopause is seen in all the temperature maps at pressures greater than 10^{-2} Pa, stronger in the autumn and winter in comparison to spring and summer, and with slightly warmer temperatures at the dawn terminator (Thiemann et al., 2018; González-Galindo et al., 2021) reaching temperatures of over ~ 170 K.

Previous work illustrating variability across latitude similarly show the mesopause with temperatures reaching less than 100 K at approximately 10^{-3}–10^{-4} Pa (Forget et al., 2009; Gröller et al., 2015). The IUVS data shown herein reveals a mesopause extending from roughly 10^{-2}–10^{-4} Pa (Figure 7, left column). The most apparent structure in the latitude temperature maps for all seasons are the warm regions occurring at pressures greater than 10^{-2} Pa (below $\sim$ 100 km). Autumn and winter seasons exhibit stronger warming at southern polar latitudes in comparison to spring and summer with temperatures exceeding 190 K. While trends in structure are observed with bin frequencies exceeding hundreds of scans in many cases, it is prudent to consider the uncertainties associated with the temperatures with respect to pressure (altitude). Binned uncertainties and the corresponding standard deviations of the binned uncertainties are provided in Figures S5 and S6, respectively, in the Supplemental Material. Temperature uncertainties may be large, with typical uncertainties at P $> 10^{-2}$ Pa from $\sim$ 31–46 K, with the larger uncertainties occurring during the dusty season (L_s = 180 - 360°). These uncertainties are representative of the individual Mars years which typically range from 30 - 45 K (at P $> 10^{-2}$ Pa), with the exception of autumn in MY34 (discussed in Section 6.3).

Results from Thiemann et al. (2018) from solar occultations during perihelion and aphelion show cooler temperatures dominating lower altitudes (below 140 km) with warmer temperatures above 200 K at higher altitudes for all latitudes. This is consistent with our dayglow observations, which yield temperatures that reach above 200 K at $\sim$ 140 km and $\lesssim$ 100 K at $\sim$ 120 km (mesopause). Nightside observations from Nakagawa et al. (2020a) show temperatures reaching down to 70 K above 100 km and temperatures of 175 K at $70 - 85$ km for latitudes $10° - 35°$ with evidence of polar warming at $75 - 90$ km from 80°–90° S. As discussed above, our findings demonstrate similar trends with cold temperatures at 120 km (mesopause) for all seasons and southern polar warming during autumn and winter. We also observe a warm region at higher pressures; however, temperatures do not consistently reach 175 K at equatorial latitudes for all conditions (Figure 7). Year-to-year trends may impact the enhancement of the feature, therefore, we discuss the equatorial warm regions below with respect to Martian year and season.

Analysis by Mars year and season yields increased validity to the interpretation above for the full mission data set. Figures $8 - 11$ show binned mean temperature maps by Martian year and season ranging from MY32 $-$ MY36. The primary result seen in mul-

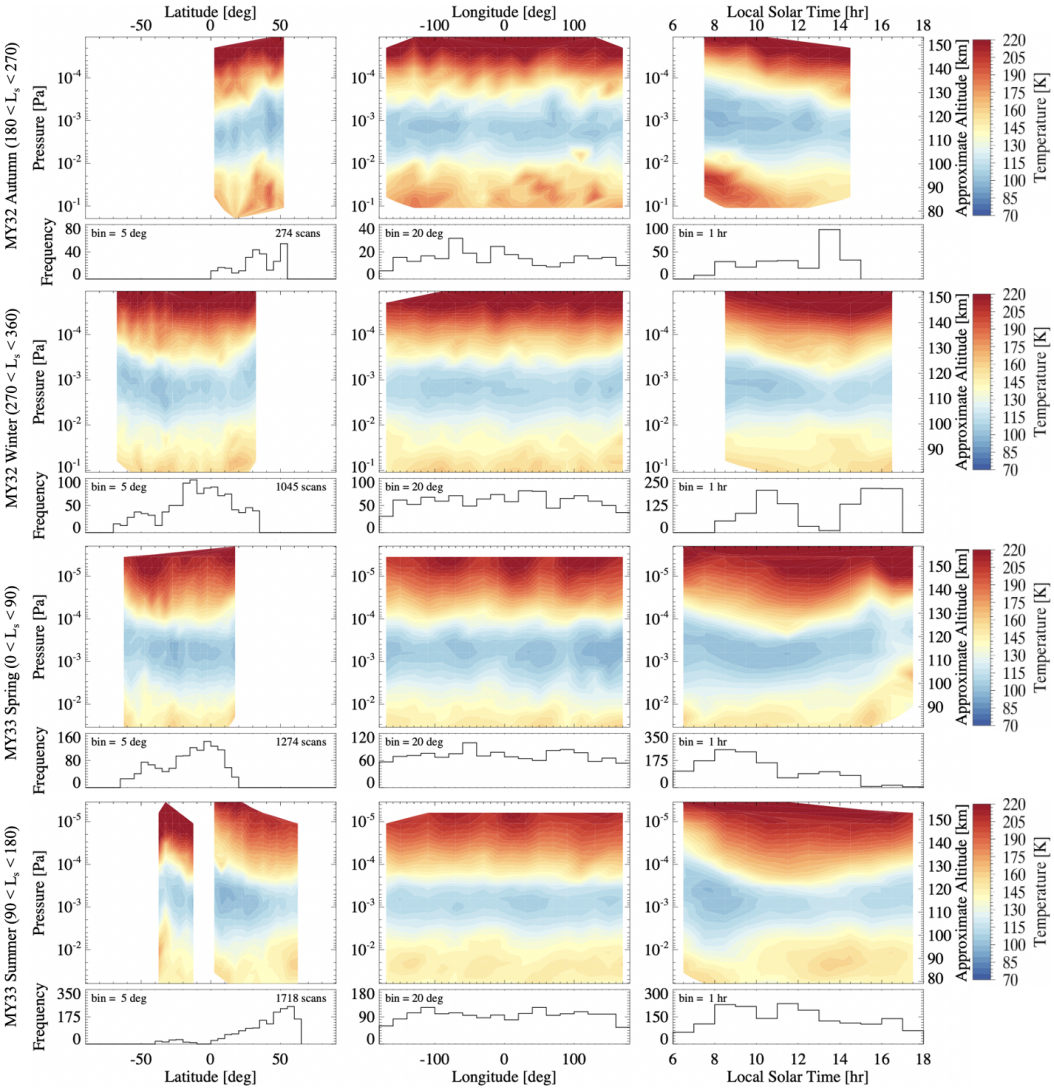

Figure 8. Thermal contour plots for the full MAVEN mission by Mars year and northern hemisphere season. From left to right, the temperature contour maps are shown as a function of pressure and approximate altitude vs latitude, longitude, and local solar time with the approximate altitude shown on the right axis. Below each contour plot is a histogram for the latitude, longitude, and local solar time for the corresponding scans. Bin sizes are indicated on the histograms. The number of limb scans included in the plot is indicated in the upper right corner of the latitude histograms. The temperatures shown are binned mean values (see Section 5.2).

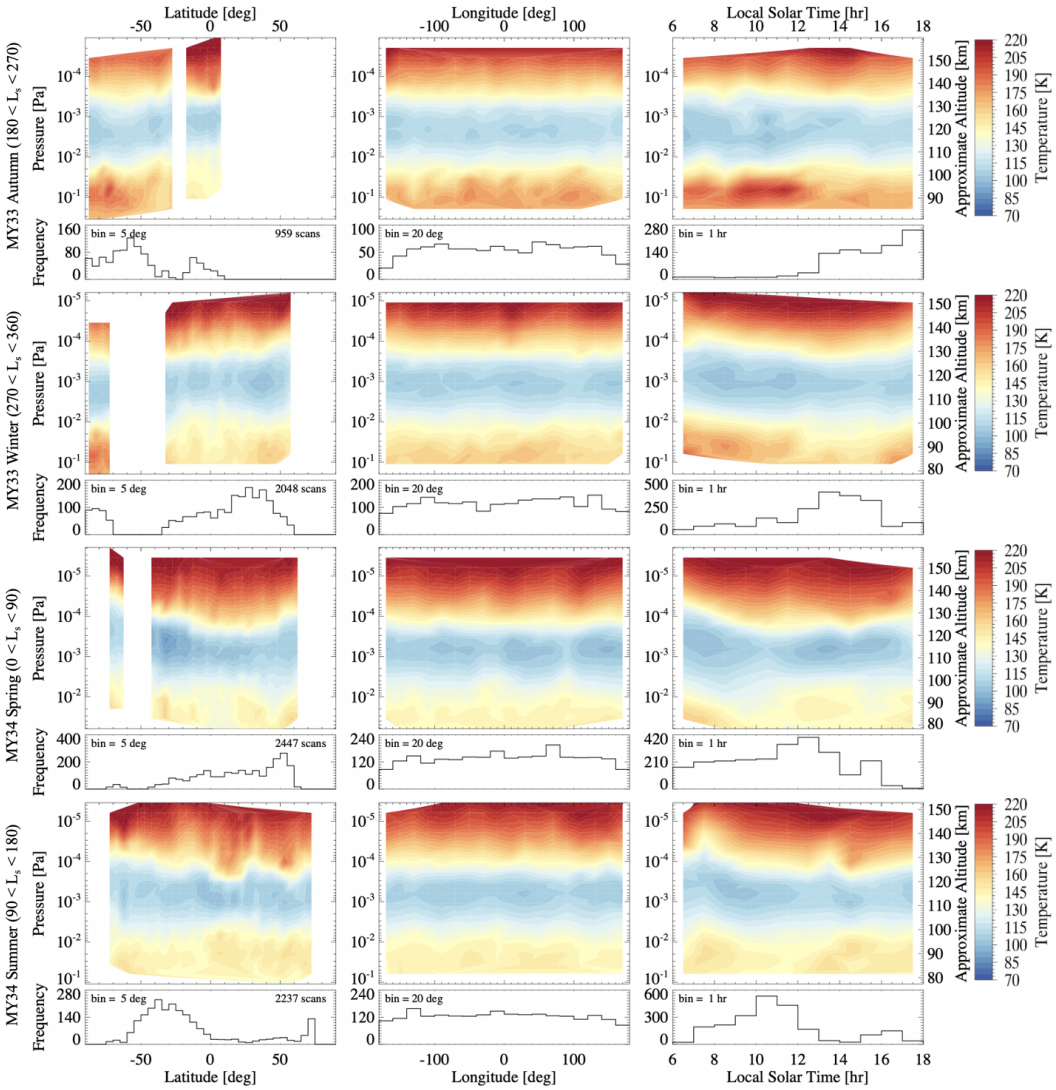

Figure 9. Continued.

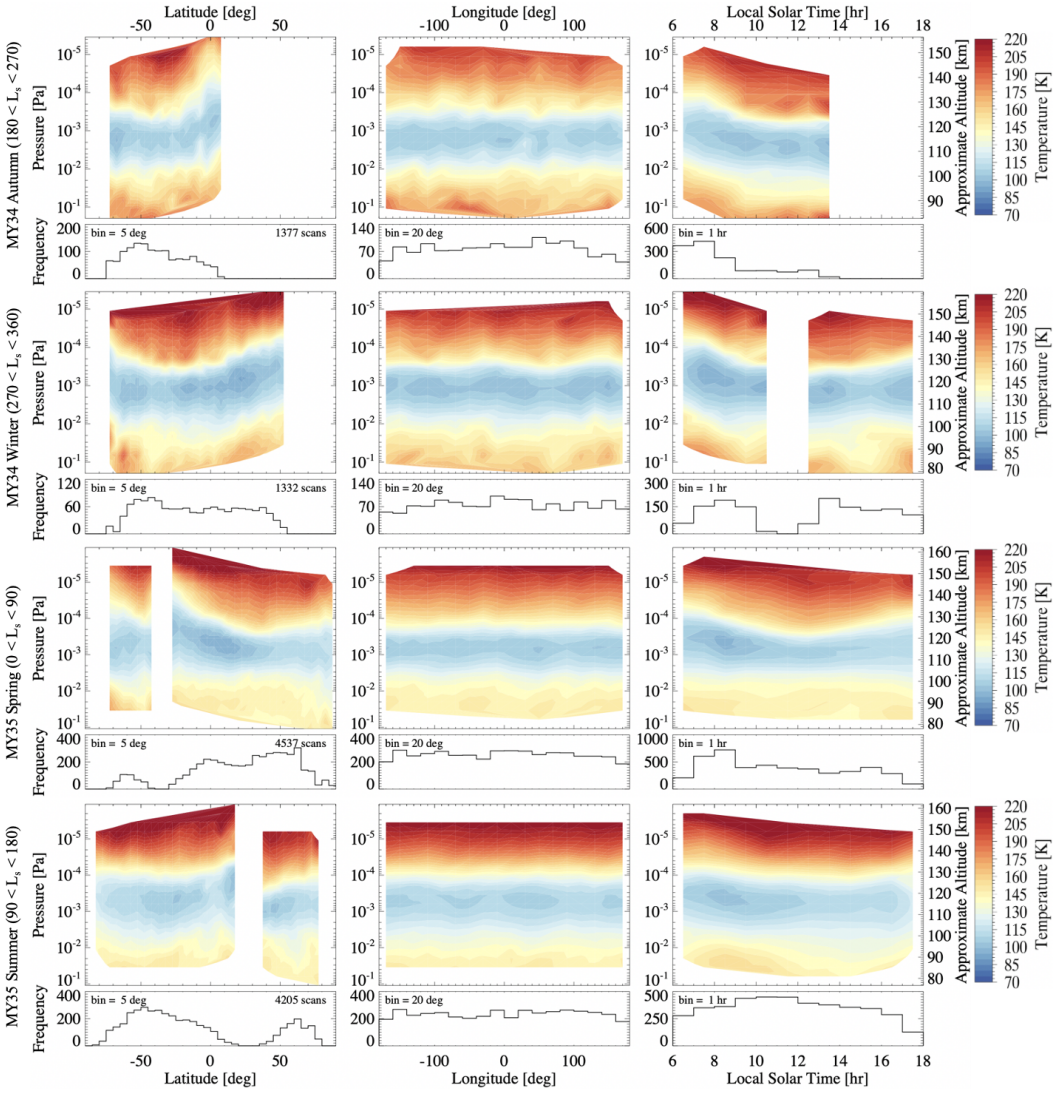

Figure 10. Continued.

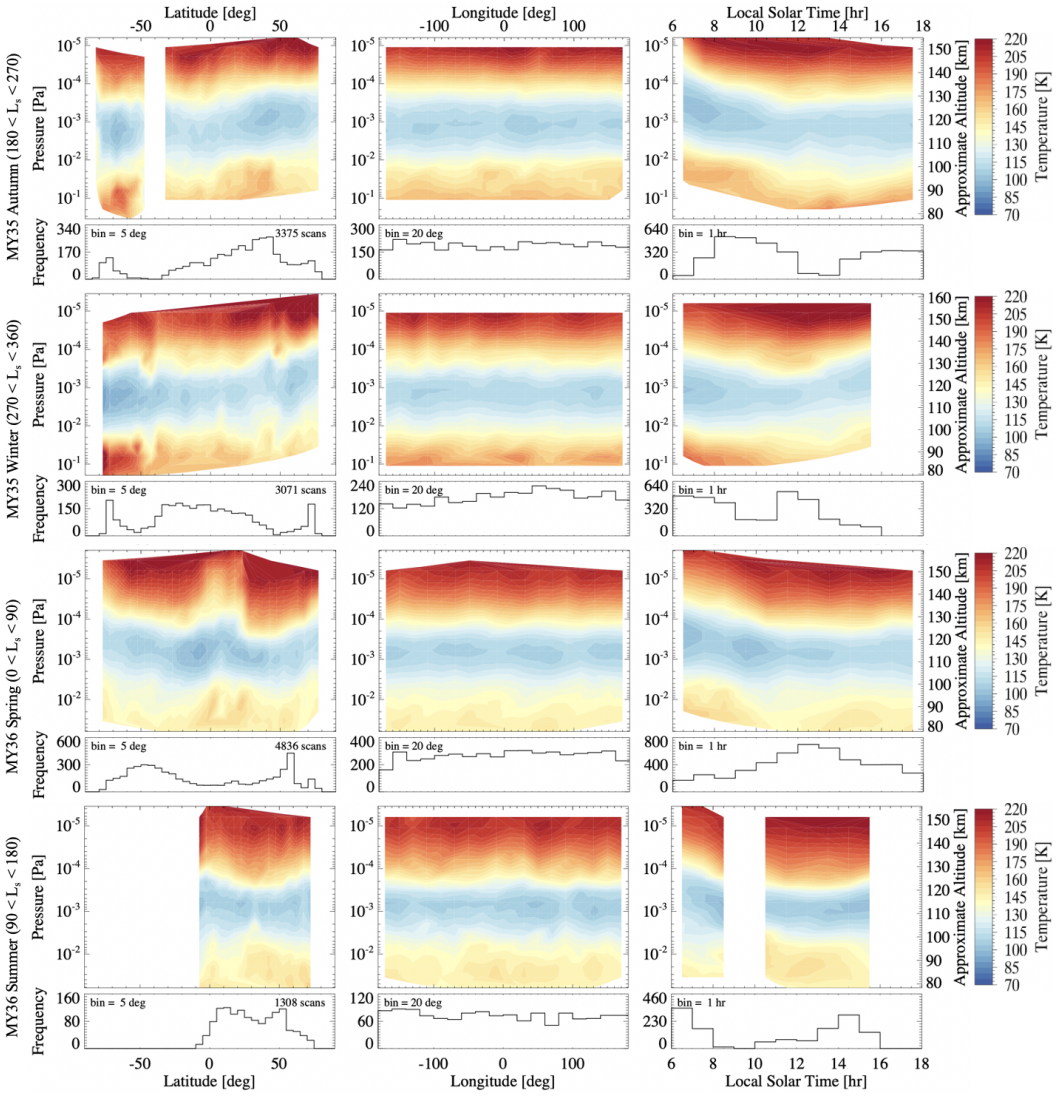

Figure 11. Continued.

tiple Martian years and across all seasons are warm regions across latitude, longitude, and LST at pressures greater than 10^{-2} Pa (below $\sim$ 100 km), as observed in the seasonal plots in Figure 7 detailed above. Many of the yearly seasonal plots exhibit higher temperatures in the warm regions during autumn and winter at southern poleward latitudes and pressures generally greater than 10^{-2} Pa (below 100 km), with upwards of 50 profiles per bin in several cases. While Figure 7 shows traces of this trend, it becomes more apparent when viewing the data by Martian year and season. The trend may be attributed to the dust season ($180° < L_s < 360°$) that occurs every Martian year during which A, B, and C regional dust events form either in the northern hemisphere (A & C) and migrate to the southern hemisphere or that form before northern winter close to the south pole (B). Nakagawa et al. (2020a) also find polar warming from $75 - 90$ km at latitudes poleward of 70° and additional warming near the equator at latitudes equatorward of 35° ($L_s = 0 - 180°$).

Temperature maps with respect to longitude show stronger warming during autumn and winter and illustrate a more well defined mesopause at consistent pressures as opposed to latitude and LST temperature maps across all seasons (Figures $8 - 11$, middle column). Some panels show interesting structures that may be attributed to longitudinal waves (discussed in further detail in Section 6.5). The yearly seasonal plots for spring and summer appear to show four concentrated regions of increased warming below 100 km in between longitudes −180° and −100°, −100° and 0°, 0° and 100°, and 100° and 180°. Some of the autumn and winter panels also appear to show warming concentrated around longitudes roughly at −100°, 0°, and 100°. These trends at higher pressures ($> 10^{-2}$ Pa) may be indicative of waves at lower altitudes. The less structurally organized warm region observed during autumn MY34 (which encompasses a global dust event) occurs at the lower limit of the temperature map at pressures greater than 10^{-2} Pa (below $\sim$ 95 km) and lower altitudes in the upper mesosphere. These could be indicative of vertically propagating thermal effects from the upper mesosphere into the lower thermosphere.

In the majority of yearly seasonal plots there is evidence of warming at pressures greater than 10^{-2} Pa (below 100 km) from the dawn terminator, slight cooling towards noon LSTs, and then warming again in the afternoon (Figures $8 - 11$, right column). These trends occur at times where the bin frequency exceeds 50 profiles (generally exceeding 100 profiles) and establishes statistical significance for the observed trend. The trend is most apparent during northern hemisphere spring and summer but also appears during several of the autumn and winter panels from MY32-MY36. Warming at the dusk and dawn terminators has been previously reported in both observations and GCMs (González-Galindo et al., 2021; Gupta et al., 2019). Gupta et al. (2019) find a dawn-dusk asymmetry using Ar, that decreases in altitude, with temperatures about 40 K warmer for dusk at 160 km for MY33 and M34. While several of the yearly seasonal plots shown in Figures $8 - 11$ appear to favor warmer temperatures at the dawn terminator, this occurs in over $\sim$ 50% of the cases, at much lower altitudes, and with typically smaller temperature gradients.

6.2 Mesopause and Warm Regions

Analysis of dayglow limb profiles and the resulting temperature profiles consistently exhibit a defined mesopause at pressures of $\lesssim 10^{-2}$ Pa (approximately 120 km) in the Martian atmosphere for a range of conditions including seasonal variations (Figures $7 - 14$). Previous observations of SPICAM and MAVEN IUVS stellar occultations at various latitudes, longitudes, and solar longitudes identified the mesopause between $100 - 130$ km and pressures less than 10^{-3} Pa (Forget et al., 2009; Gröller et al., 2015). Forget et al. (2009) found mesopause temperatures reaching down to about 70 K consistent with our daytime observations. MCD simulations from Figure 9 of Thiemann et al. (2018) illustrate similar trends to those observed in the yearly seasonal plots presented here (Fig-

ures 8 − 11). Thiemann et al. (2018) identified a well defined mesopause at ∼ 120 km with temperatures reaching 100 K and polar warming at southern latitudes below 50° S from 60 − 85 km with temperatures reaching greater than 185 K. Figures 8 − 11 also show a mesopause at approximately 120 km with temperatures reaching below 100 K; however, polar warming is observed at higher altitudes (lower pressures) in only a few of the autumn and winter panels. On Earth, the mesopause anomaly (cooler mesopause in the summer than winter) is due to upwelling at the summer pole and downwelling at the winter pole from circulation (Garcia & Solomon, 1985). Simulations from Yiğit et al. (2018) find a similar phenomena at Mars where the mesopause becomes colder with the minimum temperature shifting to the summer hemisphere. They suggest that it is due to the wind distribution and find that zonal jets reverse their directions near the mesopause, possibly due to gravity waves.

Figure 6 shows the CO_2 density and temperature profiles for two limb scans and highlights the thermal structures captured within the profiles. The scans depicted in Figure 6 are the 1^{st} scan of inbound orbit 3468 (11 July 2016 at 00:57 UTC), when there is no warm layer (left), and the 8^{th} scan of periapse orbit 14533 (8 August 2021 at 21:38 UTC), when a warm layer is present (right). The CO_2 density profile for the warm layer case has slight oscillations below 115 km in comparison to the case with no warm layer and exhibits a peak temperature of 194.0 ± 15.7 K at an altitude of 95 km ($\sim 10^{-2}$ Pa). However, for the case with no clear warm layer, the temperature does not exceed 160 K below the mesopause down to 75 km. Orbit 14533, illustrating the enhanced warm layer, is a typical profile with a change in temperature of over 65 K from the lower boundary at 75 km extending upward to 105 km. Limb profiles with like conditions will result in similar temperature profiles.

Table 2. Martian Dust Storm Events[a]

Mars year	Solar Longitude (deg)	Storm Type
MY32	$218 \leq L_s \leq 251$	Regional A
MY32	$250 \leq L_s \leq 293$	Regional B
MY33	$217.8 \leq L_s \leq 230$	Regional A
MY33	$249.9 \leq L_s \leq 291.7$	Regional B
MY34	$188 \leq L_s \leq 300$	Planetary
MY34	$249.5 \leq L_s \leq 294.4$	Regional B
MY34	$320.6 \leq L_s \leq 336.5$	Regional C
MY35	$226.6 \leq L_s \leq 259$	Regional A
MY35	$257.6 \leq L_s \leq 293.7$	Regional B
MY35	$316.1 \leq L_s \leq 329.9$	Regional C

[a] Dust events are obtained from the LASP MAVEN Data Science Center Events webpage (`https://lasp.colorado.edu/maven/sdc/public/pages/notebook/events/index.html#/`).

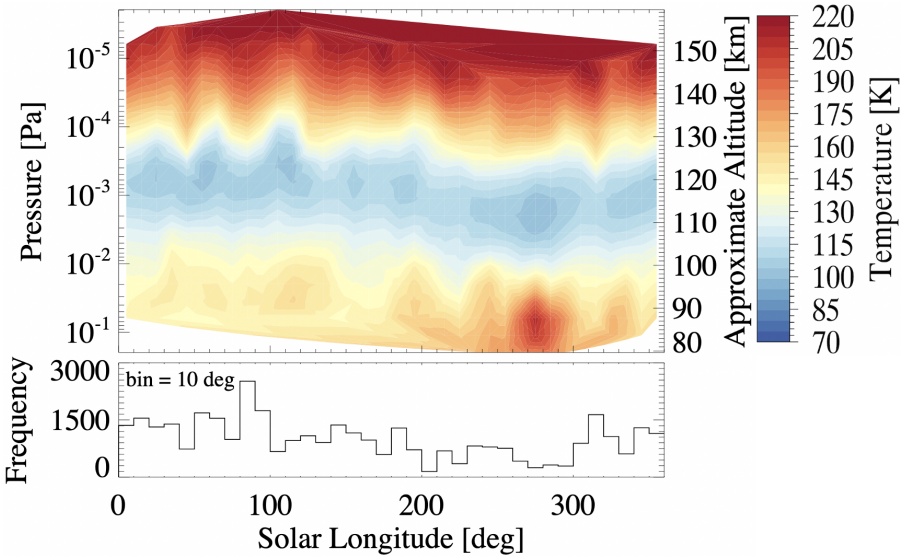

Figure 12. Thermal contour map with respect to solar longitude for the full data set (over 36,000 scans) within the constraints detailed in Section 5 for MY32-MY36 with a bin size of 10°. Below the contour plot is a histogram of the solar longitude for the corresponding scans. The temperatures shown are binned mean values (see Section 5.2).

6.3 Dust Storm Temperature Variability

The Martian dust storm season extends from $L_s = 180°$ to 360° during which regional and planetary engulfing dust storms can form. We examine dust storms from MY32 − MY36, including the planetary engulfing dust event (PEDE) of MY34. Regional and planetary dust events for MY32 − MY36 from the LASP MAVEN Data Science Center Events page are listed in Table 2. Figure 12 includes scans from all latitudes, longitudes, and MYs in the data set and demonstrates an enhanced warm region that occurs during dust season at high pressures (below ∼ 95 km; Fedorova et al., 2020; Wolkenberg et al., 2020; Steele et al., 2021). While temperature uncertainties may be larger during this period (Supplemental Materials, Figure S7), the frequency of scans in each bin is also large, thus we consider the higher temperatures to be statistically significant. Ten dust storms have been identified since the inception of the mission; however, we do not always have the necessary L_s coverage to produce the detailed thermal contour maps presented in this work. Therefore, we focus our discussion on the MY34 C regional dust event (RDE) at $320.6° \leq L_s \leq 336.5°$ (Figure 13), the B RDE observed during autumn of MY33 at $249.9° \leq L_s \leq 291.7°$ (Figure 9), and the MY34 PEDE at $188° \leq L_s \leq 300°$ (Figure 14).

Figure 13 illustrates the thermal variability during MY34 C RDE and shows a warm region at $P \gtrsim 3{\times}10^{-2}$ Pa ($\lesssim$ 95 km) in all the contour maps. The event is comprised of over 130 profiles and a minimum of 5 profiles per bin per geographic or temporal coordinate. In each temperature map, the warm region is consistently seen lower in the atmosphere along the full range of the corresponding geophysical parameter, further demonstrating that the phenomena is not an artifact but a real observed trend. Temperatures in the warmer region reach upwards of 180 K in the latitude, longitude, and L_s maps, and upwards of 170 K in the LST map with mean temperature uncertainties of ∼20 K between 80 − 150 km. However, it is important to note that mean uncertainties can be large at high pressures (∼ 60 K). Corresponding mean uncertainties for Figure 13 are shown in Figure S8 of the Supplemental Materials. The various peak temperatures re-

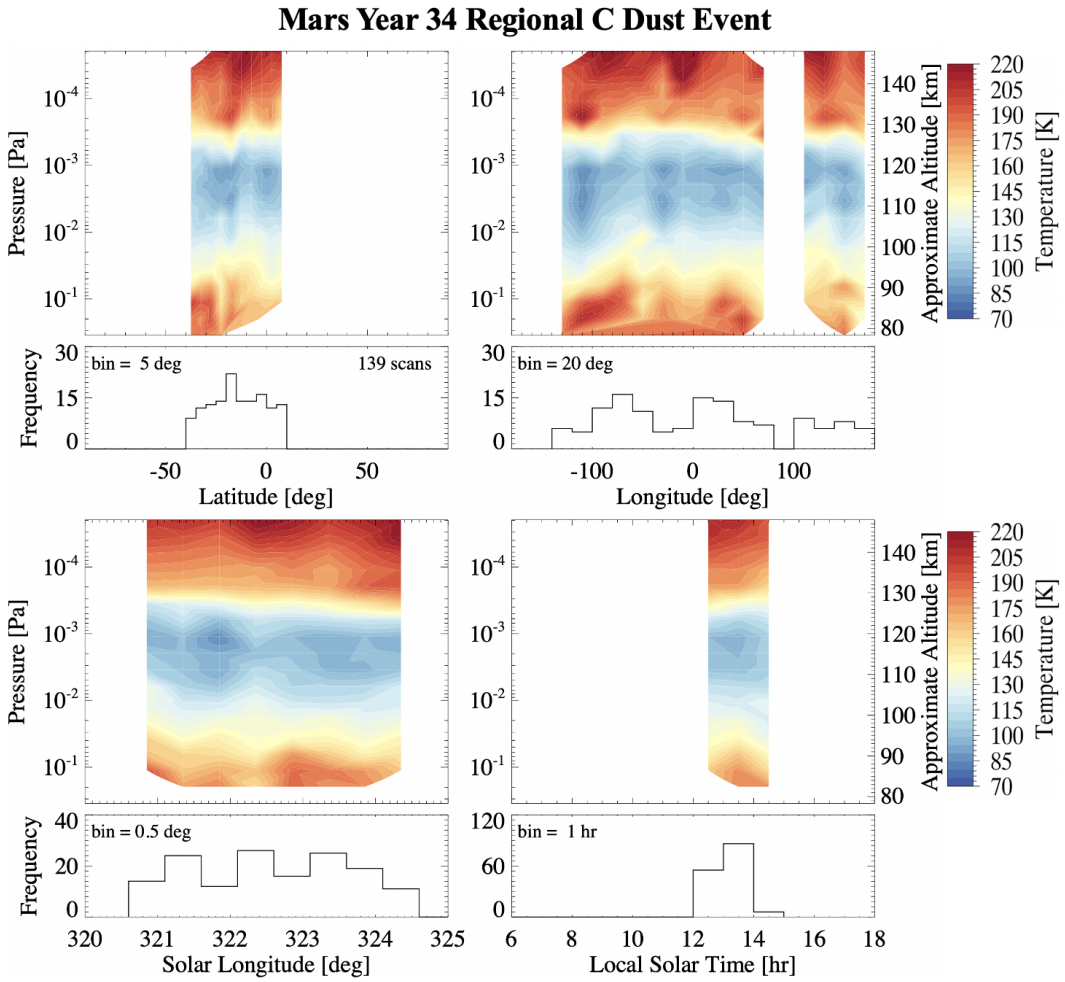

Figure 13. MY34 Regional C Dust Event. Contour plots of temperature binned with respect to latitude (top left), longitude (top right), solar longitude (bottom left) and local solar time (bottom right) are shown. The corresponding histograms and bin size are below each contour plot. Mean temperature uncertainties are ∼20 K. The temperatures shown are binned mean values (see Section 5.2).

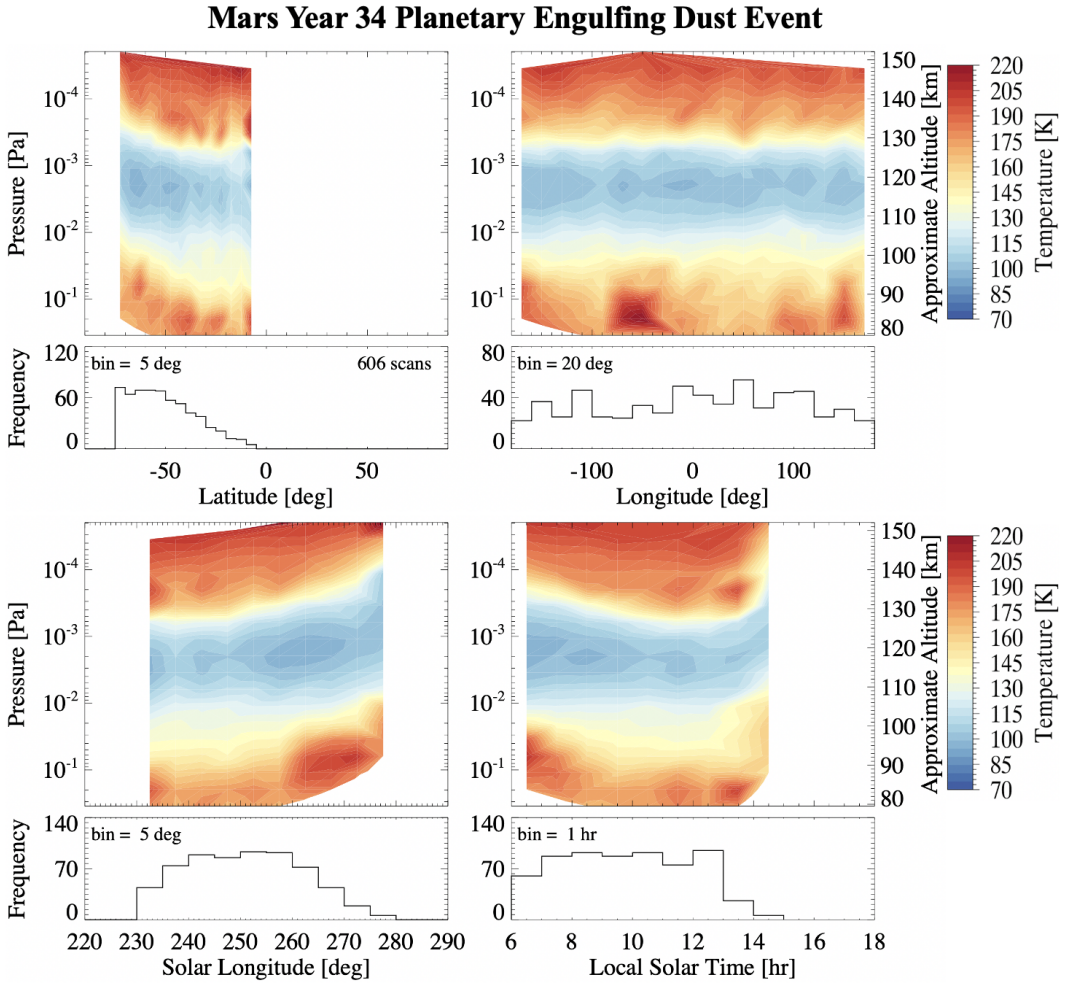

Figure 14. MY34 Planetary Engulfing Dust Event. Contour plots of the temperature binned with respect to latitude (top left), longitude (top right), solar longitude (bottom left) and local solar time (bottom right) are shown. The corresponding histograms and bin size are below each contour plot. The temperatures shown are binned mean values (see Section 5.2).

ported for the dust event differ because the data are binned differently for each parameter (as noted in the corresponding histograms shown in Figure 13). The plots for autumn MY33 shown in the top row of Figure 9 are generated with data obtained during the MY33 B RDE ($249.9° \leq L_s \leq 291.7°$). We isolate the regions of the latitude plot that correspond to this event and find a warm region at altitudes below 100 km ($P > 2{\times}10^{-2}$ Pa) and latitudes $\sim -26°$ to $-87°$ reaching temperatures of over 180 K. This demonstrates that thermal perturbations in the atmosphere due to dust activity may propagate vertically creating warmer regions higher into the lower thermosphere and at low to mid latitudes.

Figure 14 shows temperature maps for the MY34 PEDE of 2018, the first global dust storm event since MAVEN went into orbit. As indicated by the bottom left panel of Figure 14, the temperature maps illustrate the waning phase of the storm after the most active period at $L_s \sim 225°$. Each temperature map shows a warm region at high pressures ($> 2{\times}10^{-2}$ Pa, less than ~ 100 km) across the range of parameters presented, similar to the MY34 C RDE discussed above. A warm region occurs at all southern lat-

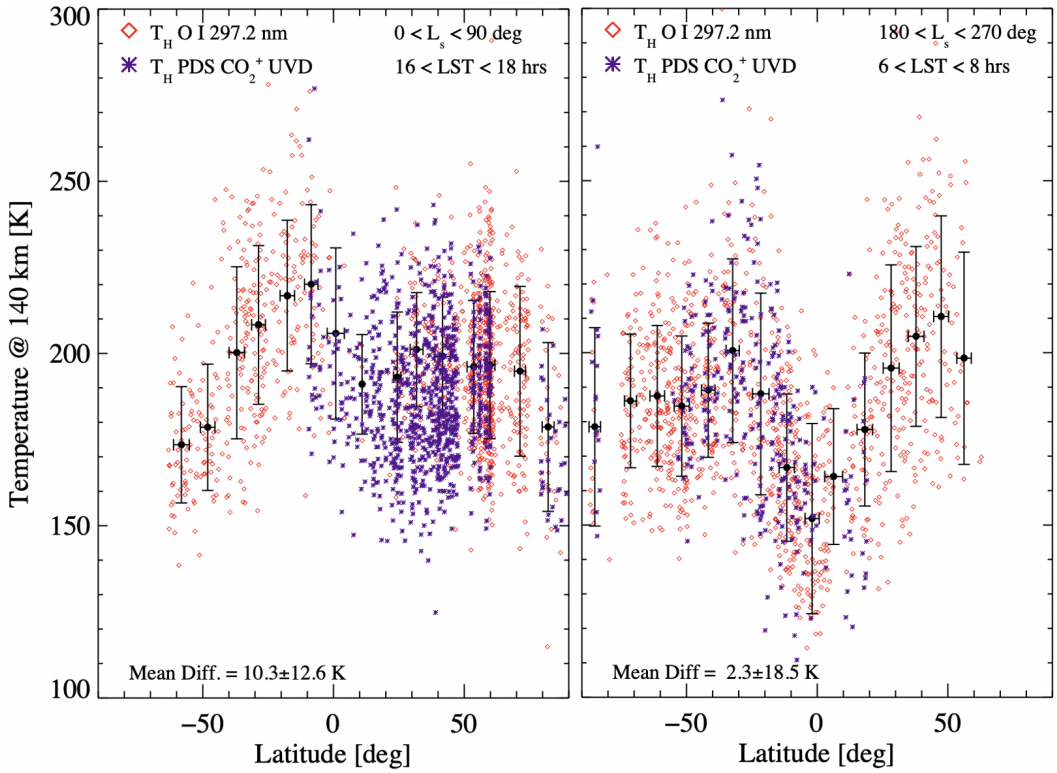

Figure 15. Temperatures derived via hydrostatic integration (T_H) for O I 297.2 nm and CO_2^+ UVD are given for inbound, outbound, and periapse orbits during northern hemisphere spring at dusk (left; $0° < L_s < 90°$, LST = 16 - 18 hrs) and autumn at the dawn terminator (right; $180° < L_s < 270°$, LST = 6 - 8 hrs) for MY32-MY36. The red diamonds are the retrieved temperatures from hydrostatic integration for the upper peak (at tangent altitude 140 km) of O I 297.2 nm. The purple asterisks are the retrieved temperatures from hydrostatic integration for CO_2^+ UVD from periapse limb scans at a tangent altitude of 140 km available from Level 2 data on the NASA Planetary Data System. The black circles are the binned mean temperatures from O I 297.2 nm with a bin size of 10° in latitude and error bars showing 1-σ std. dev. The mean temperature difference and std. dev. for corresponding periapse limb scans between the two methods is provided.

itudes extending from high in the mesosphere to low in the thermosphere, reaching temperatures over 190 K with bin frequencies typically exceeding 40 scans. Peak temperatures with respect to longitude, LST, and L_s also exceed 190 K at high pressures ($<$ 100 km). However, mean uncertainties can be large in this regime, $\sim$ 60 K, and are illustrated in Figure S9 of the Supplemental Materials. González-Galindo et al. (2015) studied the PEDE in MY25, which occurred during similar L_s to the PEDE in MY34, and showed that circulation gets damped in the thermosphere due to the development of dust storms thus modifying thermospheric temperatures. They found a strong increase in temperature at latitudes equatorward of 60°. Jain et al. (2020) also observed higher temperatures near the equator and in the afternoon during the MY34 PEDE with MAVEN IUVS observations; however, at higher altitudes. These trends are observed in Figure 14 with warmer temperatures from 50° S to 10° S and LST = 11 − 14 hrs.

Figure 3 of Jain et al. (2020) shows thermospheric temperatures at $\sim$ 170 km from IUVS data binned in solar longitude and latitude, similar to Figure 15 presented here, which includes temperatures from all limb scans during northern autumn and spring near the dawn and dusk terminators that meet the criteria described in Section 5. The figure demonstrates the consistency in retrieved temperatures at 140 km obtained via hydrostatic integration for IUVS observations of CO_2^+ UVD and the upper peak of O I 297.2 nm. The mean temperature difference determined from periapse limb scan observations of CO_2^+ UVD and the upper peak of O I 297.2 nm are 10.3 K (spring dusk; Figure 15 left) and 2.3 K (autumn dawn; Figure 15 right) and have $1-\sigma$ standard deviations of 12.6 K and 18.5 K, respectively. The decreasing temperatures approaching lat = 0° with an upturn at northern latitudes observed in Jain et al. (2020) for the MY34 PEDE is clearly seen in the right panel of Figure 15 for LSTs near dawn during northern hemisphere autumn, which is part of dust storm season. A similar trend was observed in Jain et al. (2021) during solar minimum, shifted to lower latitudes, and is attributed to meridional effects. Recent studies using the ExoMars Trace Gas Orbiter found high water vapor abundances in the middle atmosphere at altitudes up to 100 km from 60° S to 60° N during the MY34 PEDE that resulted from warmer temperatures lower in the mesosphere (Aoki et al., 2019; Neary et al., 2020; Vandaele et al., 2019). The latitudinal variation of water vapor exhibits similar trends to Figure 15 and is likewise attributed to the seasonal change of meridional circulation: from a two to one cell Hadley circulation (Aoki et al., 2019; Neary et al., 2020).

6.4 Latitudinal Variability

Thermal variability with respect to latitude is observed in Figures 7 − 14; however, the variability often encompasses a large range in longitude, L_s, and LST. Figure 15 illustrates trends where the latitudinal variability is decoupled from other geophysical parameters. Figure 15 shows hydrostatic integration temperatures at a tangent altitude of 140 km derived via O I 297.2 nm and CO_2^+ UVD emission during northern hemisphere spring and autumn for LSTs constrained within a 2 hr bin near the dusk and dawn terminators, respectively. During the spring, mean binned O I 297.2 nm temperatures increase equatorward from 173 K at 58° S, reaching 220 K at 8° S, and decreasing to 179 K at 82° N. The trend reveals a downward parabolic shape with regards to the thermal variability. In the autumn, the opposite is observed near the dawn terminator (LST = 6 - 8 hrs) with mean binned temperatures decreasing by $\sim$ 50 K as they approach Lat = 0°. The binned temperatures drop from 201 K at 32° S to 152 K at 2° S and then increase again to about 210 K at 47° N. The drop in temperature is also demonstrated in the UVD derived temperatures.

The thermal variability observed near dusk is consistent with NGIMS dayside results from Stone et al. (2022) while the asymmetry observed near the dawn terminator is reminiscent of latitudinal variability seen in Jain et al. (2021) at LST = 8 − 10 hr with a 20 K thermal drop centered around 20° S. The polar warming at dawn (McCleese et

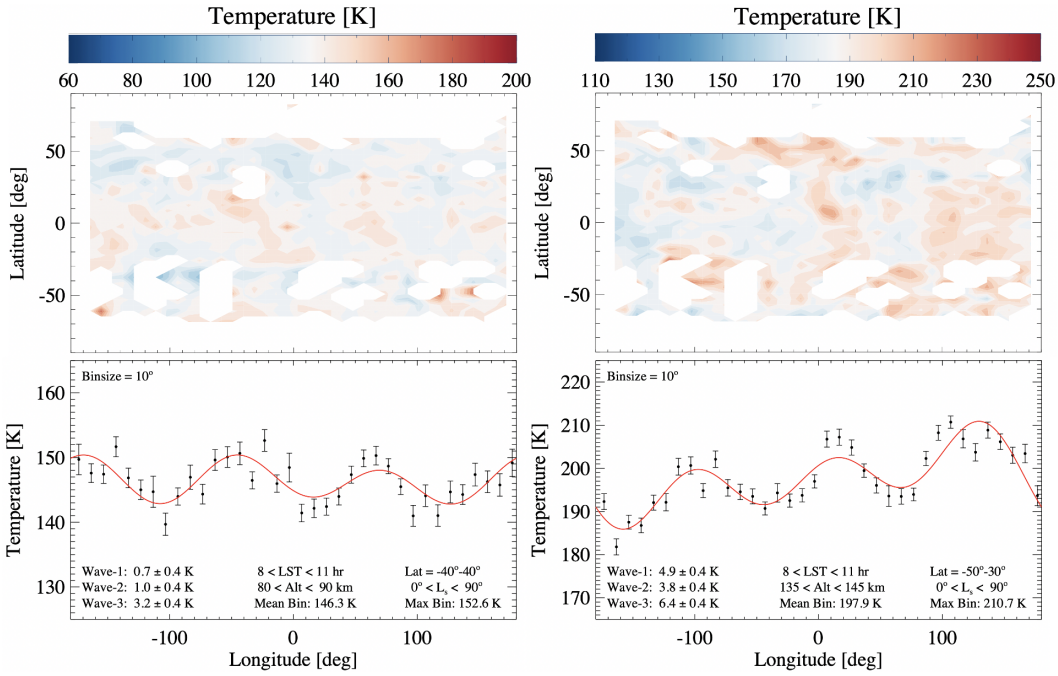

Figure 16. (Top) Latitude vs longitude temperature maps for northern spring ($0^\circ < L_s < 90^\circ$) constrained to 8 < LST < 11 hrs. Temperatures shown at 80 < alt < 90 km (left) and 135 < alt < 145 km (right), binned in latitude (bin size = 5°) and longitude (bin size = 10°). (Bottom) Temperature vs longitude for latitudes −40° to 40° (left) and −50° to 30° (right). Binned mean temperatures (bin size = 10°) and the corresponding standard error of the mean are shown in black. The red curve is the fit to the data. The temperatures shown are binned mean values (see Section 5.2).

al., 2008) may be caused by downwelling in the polar morning region. Nakagawa et al. (2020b) demonstrate a similar pattern of warming near the southern polar region, cooling equatorward, and warming toward northern high latitudes; however, at ∼80-90 km and during northern spring/summer (L_s = 0 - 180°). Likewise, enhanced warming appears near the equator at approximately 100 km; however, at northern autumn/winter (L_s = 180 - 360°), with cooler temperatures at high northern and southern latitudes. As suggested by Nakagawa et al. (2020b), upward propagating waves may create a turbulent layer that induce vertical mixing and influence the thermospheric composition.

6.5 Longitudinal Waves and Tides

Several temperature maps binned in longitude (middle column of Figures 7 − 11) demonstrate patterns of wave activity for all seasons and Martian years, during both quiet and active dust periods (Figures 13 − 14). The longitude maps demonstrate turbulent behavior with intermittent periods of heating and cooling indicative of wave structures. Alternating periods of cool and warm temperatures below approximately 100 km also demonstrate wave features. Above the mesopause, between approximately 130 − 140 km, strong warming alternates with cooling indicating wave activity as well. The longitudinal structures above 100 km may be a result of tidal influences originating near the surface during the dust storm that modulates the upper atmosphere. As suggested by Starichenko et al. (2021), the vertical temperature perturbations could be showing gravity waves, which dissipate in the mesopause and induce temperature fluctuations.

Temperature maps for northern spring (quiet dust period) with respect to longitude and latitude are presented in Figure 16 (upper panels) for upper mesospheric altitudes (80 − 90 km) and lower thermospheric altitudes (135 − 145 km) exhibit warm regions near the equator. The perturbations with respect to longitude reflect a wave-like pattern that is similar to the wavenumber-3 structure of non-migrating tides found in the thermosphere for both temperatures and CO_2 densities (Withers et al., 2003; Lo et al., 2015; Medvedev et al., 2016; Stevens et al., 2017; England et al., 2019; Thaller et al., 2020; Jain et al., 2021). Temperatures constrained within a 3 hr LST bin and in latitude, are averaged to illustrate longitudinal variations, with least squares fit to the data as detailed in Jain et al. (2021) and Lo et al. (2015).

We show the wavenumber-1 to -3 amplitudes in the bottom row of Figure 16, which have been determined using a Levenberg-Marquardt least square fit following Equation 2 of Jain et al. (2021). Nakagawa et al. (2020a) find a wave-3 amplitude of 9.9 K for combined northern spring and summer seasons at Lat = $0 - 50^\circ$ N between $75 - 85$ km. While the wave amplitude at lower altitudes is about 1/3 (3.2 K) for the spring, it does exhibit a dominant wave-3 component as reported by Nakagawa et al. (2020a). At higher altitudes the temperatures are $\sim$ 51 K warmer and the wave-3 component dominates followed by wave-1 and wave-2 components similar to trends observed by England et al. (2019) at altitudes of $150 - 175$ km.

We stress that quantitative comparisons with results derived from other data sets or models can be challenging, particularly when attempting to utilize coincident or collocated data sets, therefore such studies should be done carefully and cautiously. Finally, we note that the maxima in Figure 16 (bottom) occur at longitudes 69° (148.0 K), -45° (150.4 K), and -170° (150.4 K) for the fit to temperatures at $80 <$ alt < 90 km and 129° (210.9 K), 16° (202.5 K), and -97° (199.7 K) for the fit to temperatures at $135 <$ alt < 145 km. The global maxima of the lower and upper atmospheric longitudinal waves are therefore about 65° out of phase (Figure 16, bottom), and while this is an interesting finding, a detailed analysis of the phenomena is beyond the scope of this paper and will be addressed in a future analysis.

7 Conclusions

In this study, we have presented four Martian years of data spanning from MY32 to MY36 (October 2014 to November 2021) and have investigated dayside lower thermospheric and upper mesospheric O I 297.2 nm temperatures derived via hydrostatic integration using MAVEN IUVS limb scan observations. We provide a detailed explanation of the models and algorithms implemented to retrieve CO_2 number density profiles and derive corresponding temperatures with formally propagated errors. An important advance in this work is the inclusion of inbound and outbound limb scans on either side of nominal periapse limb scans, which increases the number of profiles for analysis by 37%. We show that the retrieved CO_2 number densities and temperatures of the upper peak ($\sim$120 km) obtained using the O I 297.2 nm emission are consistent with results obtained by MAVEN IUVS operational retrievals using CO_2^+ UVD emissions. We find that derived temperature maps are consistent with GCM predictions under similar geophysical conditions (Thiemann et al., 2018; Gupta et al., 2019).

We show for the first time temperature profiles from 80 to 150 km obtained from MAVEN IUVS observations of O I 297.2 nm emission. This extends the IUVS operational CO_2 density and temperature product that is currently reported between $130 -$ 170 km. This new O I 297.2 nm analysis enables us to bridge the gap and improve our understanding of the coupling that occurs between the upper mesopshere and thermosphere of Mars. We find that patterns in temperature variability persist across all seasons and Mars years. Four key findings of this paper are: (1) the identification of the mesopause at P $\approx 10^{-3}-10^{-2}$ Pa ($\sim$ 120 km), (2) warming at high pressures ($> 10^{-2}$ Pa, below

~100 km) across latitude, longitude, and LST for a variety of geophysical conditions, (3) asymmetry in temperatures near the dawn and dusk terminators with respect to latitude and season, and (4) longitudinal waves observed during both quiet and active dust periods, with lower (80 − 90 km) and upper (135 − 145 km) atmospheric waves about 65° out of phase.

Thermal variability at low altitudes with respect to latitude could indicate circulation or the impact of gravity waves. A study conducted during the second half of MY34 ($L_s = 165°-355°$) observed enhanced gravity wave dissipation in the mesopause which induced temperature fluctuations (Starichenko et al., 2021). Gravity waves may also contribute to the southern polar warming observed at autumn and winter seasons. GCM simulations from Yiğit et al. (2018) found that gravity wave induced temperature fluctuations dominate from 100 − 140 km, primarily over the equator and at high latitudes. Therefore we could be observing the impact of gravity waves over these regions; however, a thorough analysis of this hypothesis is beyond the scope of this paper.

It is clear that understanding the coupling between the thermosphere and upper mesosphere impacted by variability driven by LST changes, longitudinal waves, and gravity waves is crucial to our ability to characterize the Martian atmosphere and drivers of thermal escape. While our analysis focused on key general trends in the thermal behavior between the mesosphere and thermosphere, these data and future observations are necessary to constrain models and wave activity, and essential to characterize the vertical distribution and the loss of water and its constituents.

Our analysis has revealed thermal variability in the Martian atmosphere from 80 to 150 km with respect to latitude, longitude, local time, season, dust activity, and solar activity. As suggested by previous studies, gravity waves generated in the lower atmosphere propagate to the thermosphere, coupling the atmospheric layers, and produce fluctuations in density (up to 40% locally) that can affect the background atmospheric temperature, which is a key parameter driving thermal escape when the H flux into the upper atmosphere is not limited by diffusion lower down (Yiğit et al., 2021; Yiğit, 2021). The density and temperature data presented here provide an important but heretofore missing source of information that is needed to directly link weather and waves in the lower atmosphere to perturbations in composition and temperature in the upper atmosphere.

Acknowledgments

This research was supported by NASA through the MAVEN project.

Appendix A Temperature Derivation

Temperature profiles are derived for CO_2 at Mars utilizing an initial temperature estimate at the top of the atmosphere (T_0, taken from the Chapman fit to the brightness profile with a lower limit of 50 K), a density profile (N), radial altitude (r) and planetary data including the molecular mass number (m), mass of Mars (M_P), and radius of Mars. To determine a temperature profile, we utilize the retrieved density profile, which is known at discrete altitudes, and assume that the atmosphere is in hydrostatic equilibrium.

$$P_j = P_{j-1} + W_j/A_j = P_{j-1} + W_j/4\pi r_j^2 \tag{A1}$$

where,

$$W_j = \int_{r_{j-1}}^{r_j} \frac{N(r)GmM_P}{r^2} 4\pi r^2 dr \tag{A2}$$

The pressure at the bottom of each lower altitude layer (P_j) is given by the pressure at the top of the layer (P_{j-1}) plus the weight of the species in the volume of the layer (W_j) divided by the area (A_j). Assuming that the volume element is nearly cylindrical, we can consider a layer j with a density N_j that varies exponentially over the layer.

$$N(r) = N_j = N_{j-1} e^{(r-r_{j-1})\frac{lnN_j - lnN_{j-1}}{r_j - r_{j-1}}} \tag{A3}$$

Therefore, Equation A1 may be re-written as,

$$P_j = P_{j-1} + \frac{GmM_p}{C_j \bar{r_j}^2}(N_j - N_{j-1}) \tag{A4}$$

where,

$$C_j \equiv \frac{lnN_j - lnN_{j-1}}{r_j - r_{j-1}} \tag{A5}$$

and

$$\bar{r_j}^2 = \left(\frac{r_{j-1} + r_j}{2}\right)^2 \tag{A6}$$

This can be further simplified by grouping together constants including $\bar{r_j}$, which is constant as a result of the altitude grid produced from the density retrieval, into β_j.

$$\beta_j = \frac{GmM_p}{\bar{r_j}^2} \tag{A7}$$

Equation A4 can therefore be expressed as,

$$P_j = P_{j-1} + \frac{\beta_j}{C_j}(N_j - N_{j-1}) \tag{A8}$$

and can be further simplified to

$$P_j = P_{j-1} + D_j \text{ where } D_j = \frac{\beta_j}{C_j}(N_j - N_{j-1}) \tag{A9}$$

The temperature at each altitude layer may then be calculated using the following equation, where k is Boltzmann's constant.

$$T_j = P_j / kN_j \tag{A10}$$

Appendix B Temperature Uncertainty Derivation

Uncertainties in derived temperature profiles are obtained from the corresponding uncertainties in the retrieved density profiles. We perform formal error propagation of the density uncertainties through Equation A10, which takes into account the assumed *a priori* uncertainties used in the density retrieval algorithm as well as the upper boundary condition used for hydrostatic integration of the density profiles. The uncertainties in derived temperatures can be formally expressed as,

$$\sigma_{T_j}^2 = \sigma_{N_j}^2 \left(\frac{\partial T_j}{\partial N_j}\right)^2 + \sigma_{P_j}^2 \left(\frac{\partial T_j}{\partial P_j}\right)^2 \quad (j \geq 1) \tag{B1}$$

where,

$$\sigma_{P_j}^2 = \sigma_{T_0}^2 \left(\frac{\partial P_j}{\partial T_0}\right)^2 + \sum_{k=0}^{k=j} \sigma_{N_k}^2 \left(\frac{\partial P_j}{\partial N_k}\right)^2 + \sum_{k=1}^{k=j} \sum_{i=0}^{i=k-1} 2\sigma_{N_i N_k}^2 \left(\frac{\partial P_j}{\partial N_i}\right)\left(\frac{\partial P_j}{\partial N_k}\right) \tag{B2}$$

The partials in Equation B2 are given as follows:

$$P_0 = kN_0T_0 \qquad \frac{\partial P_0}{\partial N_0} = kT_0 \qquad \frac{\partial P_j}{\partial T_0} = \frac{\partial P_0}{\partial T_0} = kN_0 \tag{B3}$$

where are N_0 is the density at the top of the profile, T_0 is determined from the Chapman fit to the brightness profile, σ_{T_0} is the uncertainty for the temperature determined from the Chapman fit, and

$$\frac{\partial P_j}{\partial N_k} = \frac{\partial P_{k+1}}{\partial N_k} \quad (k \leq j-2) \tag{B4}$$

$$\frac{\partial P_j}{\partial N_j} = \frac{\beta_j}{C_j} - \frac{\beta_j}{C_j^2} \frac{(N_j - N_{j-1}}{N_j(r_{j-1} - r_j)} \quad (j \geq 1) \tag{B5}$$

$$\frac{\partial P_j}{\partial N_{j-1}} = \frac{\partial P_{j-1}}{\partial N_{j-1}} - \frac{\beta_j}{C_j} + \frac{\beta_j}{C_j^2} \frac{(N_j - N_{j-1}}{N_j(r_{j-1} - r_j)} \quad (j \geq 1) \tag{B6}$$

The partial derivatives of the temperature with respect to density and pressure are given by,

$$\frac{\partial T_j}{\partial N_j} = -\frac{P_j}{kN_j^2} \qquad \frac{\partial T_j}{\partial P_j} = \frac{1}{kN_j} \tag{B7}$$

Here σ_{N_k} and $\sigma_{N_i N_k}$ are the associated uncertainties in the density.

Open Research

Data Availability Statement

The MAVEN IUVS processed (Level 1C; Version 13 Revision 1) and derived (Level 2; Version 13 Revision 1) data are publicly available in FITS format on the NASA Planetary Data System (PDS; Deighan, 2018b, 2018a). The corresponding MAVEN EUVM (Level 3; Version 14 Revision 3) data are publicly available in CDF format (Eparvier, 2017). Retrieved CO_2 densities, derived temperatures, and dust events reported herein are publicly available in IDL SAV format (Evans et al., 2023).

References

Alge, E., Adams, N., & Smith, D. (1983). Measurements of the dissociative recombination coefficients of o2+, no+ and nh4+ in the temperature range 200-600k. *Journal of Physics B: Atomic and Molecular Physics*, *16*(8), 1433.

Aoki, S., Gkouvelis, L., Gérard, J.-C., Soret, L., Hubert, B., Lopez-Valverde, M., ... others (2022). Density and temperature of the upper mesosphere and lower thermosphere of mars retrieved from the oi 557.7 nm dayglow measured by tgo/nomad. *Journal of Geophysical Research: Planets*, e2022JE007206.

Aoki, S., Vandaele, A. C., Daerden, F., Villanueva, G. L., Liuzzi, G., Thomas, I. R., ... Lopez-Moreno, J. J. (2019, December). Water Vapor Vertical Profiles on Mars in Dust Storms Observed by TGO/NOMAD. *Journal of Geophysical Research (Planets)*, *124*(12), 3482-3497. doi: 10.1029/2019JE006109

Avakyan, S., Ii,In, R., Lavrov, V., & Ogurtsov, G. (1998, January). *Collision processes and excitation of UV emission from planetary atmospheric gases : a handbook of cross sections.*

Bishop, J., & Feldman, P. D. (2003, June). Analysis of the Astro-1/Hopkins Ultraviolet Telescope EUV-FUV dayside nadir spectral radiance measurements. *Journal of Geophysical Research (Space Physics)*, *108*(A6), 1243. doi: 10.1029/2001JA000330

Bishop, J., Stevens, M. H., & Feldman, P. D. (2007, October). Molecular nitrogen Carroll-Yoshino v' = 0 emission in the thermospheric dayglow as seen by the Far Ultraviolet Spectroscopic Explorer. *Journal of Geophysical Research (Space Physics)*, *112*(A10), A10312. doi: 10.1029/2007JA012389

Bougher, S. W., Roeten, K. J., Olsen, K., Mahaffy, P. R., Benna, M., Elrod, M., ... others (2017). The structure and variability of mars dayside thermosphere from maven ngims and iuvs measurements: Seasonal and solar activity trends in scale heights and temperatures. *Journal of Geophysical Research: Space Physics*, *122*(1), 1296–1313.

Capetanakis, F., Sondermann, F., Höser, S., & Stuhl, F. (1993). Temperature dependence of the quenching of o (1 s) by simple inorganic molecules. *The Journal of chemical physics*, *98*(10), 7883–7887.

Chaffin, M., Deighan, J., Schneider, N., & Stewart, A. (2017). Elevated atmospheric escape of atomic hydrogen from mars induced by high-altitude water. *Nature geoscience*, *10*(3), 174–178.

Connour, K., Wolff, M. J., Schneider, N. M., Deighan, J., Lefèvre, F., & Jain, S. K. (2022). Another one derives the dust: Ultraviolet dust aerosol properties retrieved from maven/iuvs data. *Icarus*, 115177.

Damian, V., Sandu, A., Damian, M., Potra, F., & Carmichael, G. R. (2002). The kinetic preprocessor kpp-a software environment for solving chemical kinetics. *Computers & Chemical Engineering*, *26*(11), 1567–1579.

Deighan, J. (2018a). *MAVEN IUVS Derived-level Data Product Bundle* [Dataset]. NASA Planetary Data System. doi: 10.17189/1518956

Deighan, J. (2018b). *MAVEN IUVS Processed-level Data Product Bundle* [Dataset]. NASA Planetary Data System. doi: 10.17189/1518964

England, S. L., Liu, G., Kumar, A., Mahaffy, P. R., Elrod, M., Benna, M., ... Evans, J. S. (2019, April). Atmospheric Tides at High Latitudes in the Martian Upper Atmosphere Observed by MAVEN and MRO. *Journal of Geophysical Research (Space Physics)*, *124*(4), 2943-2953. doi: 10.1029/2019JA026601

Eparvier, F. (2017). *MAVEN Extreme ultraviolet (EUV) Modelled Data Bundle* [Dataset]. NASA Planetary Data System. doi: 10.17189/1414173

Evans, J., Correira, J., Deighan, J., Jain, S., Al Matroushi, H., Al Mazmi, H., ... others (2022). Retrieval of co relative column abundance in the martian thermosphere from fuv disk observations by emm emus. *Geophysical Research Letters*, e2022GL099615.

Evans, J., Lumpe, J., Correira, J., Veibell, V., Kyrwonos, A., McClintock, W., ... Eastes, R. (2020). Neutral exospheric temperatures from the gold mission. *Journal of Geophysical Research: Space Physics*, *125*(9), e2020JA027814.

Evans, J., Soto, E., Jain, S. K., Deighan, J., Stevens, M. H., Chaffin, M. S., ... Curry, S. (2023). *Dayside temperature maps of the upper mesosphere and lower thermosphere of Mars retrieved from MAVEN IUVS observations of O I 297.2 nm emission* [Dataset]. University of Colorado Boulder. doi: 10.25810/1BKN-BS85

Evans, J. S., Stevens, M. H., Lumpe, J. D., Schneider, N. M., Stewart, A. I. F., Deighan, J., ... Jakosky, B. M. (2015, November). Retrieval of CO_2 and N_2 in the Martian thermosphere using dayglow observations by IUVS on MAVEN. *Geophysical Research Letters*, *42*(21), 9040-9049. doi: 10.1002/2015GL065489

Fedorova, A. A., Montmessin, F., Korablev, O., Luginin, M., Trokhimovskiy, A., Belyaev, D. A., ... others (2020). Stormy water on mars: The distribution and saturation of atmospheric water during the dusty season. *Science*, *367*(6475), 297–300.

Fehsenfeld, F., Dunkin, D., & Ferguson, E. E. (1970). Rate constants for the reaction of co2+ with o, o2 and no; n2+ with o and no; and o2+ with no. *Planetary and Space Science*, *18*(8), 1267–1269.

Forbes, J. M., Lemoine, F. G., Bruinsma, S. L., Smith, M. D., & Zhang, X. (2008, January). Solar flux variability of Mars' exosphere densities and temperatures. *Geophysics Research Letters*, *35*(1), L01201. doi: 10.1029/2007GL031904

Forget, F., Hourdin, F., Fournier, R., Hourdin, C., Talagrand, O., Collins, M., ... Huot, J.-P. (1999). Improved general circulation models of the martian atmosphere from the surface to above 80 km. *Journal of Geophysical Research: Planets*, *104*(E10), 24155–24175.

Forget, F., Montmessin, F., Bertaux, J.-L., González-Galindo, F., Lebonnois, S., Quémerais, E., ... López-Valverde, M. A. (2009, January). Density and temperatures of the upper Martian atmosphere measured by stellar occultations with Mars Express SPICAM. *Journal of Geophysical Research (Planets)*, *114*(E1), E01004. doi: 10.1029/2008JE003086

Fox, J. L., Benna, M., McFadden, J. P., Jakosky, B. M., et al. (2021). Rate coefficients for the reactions of co2+ with o: Lessons from maven at mars. *Icarus*, *358*, 114186.

Fox, J. L., & Dalgarno, A. (1979). Ionization, luminosity, and heating of the upper atmosphere of Mars. *Journal of Geophysical Research: Space Physics*, *84*(A12), 7315-7333. doi: 10.1029/JA084iA12p07315

Fox, J. L., & Sung, K. (2001). Solar activity variations of the venus thermosphere/ionosphere. *Journal of Geophysical Research: Space Physics*, *106*(A10), 21305–21335.

Garcia, R. R., & Solomon, S. (1985, April). The effect of breaking gravity waves on the dynamics and chemical composition of the mesosphere and lower thermosphere. *Journal of Geophysics Research*, *90*(D2), 3850-3868. doi: 10.1029/JD090iD02p03850

Gérard, J.-C., Aoki, S., Willame, Y., Gkouvelis, L., Depiesse, C., Thomas, I., ...

others (2020). Detection of green line emission in the dayside atmosphere of mars from nomad-tgo observations. *Nature Astronomy*, *4*(11), 1049–1052.

Gkouvelis, L., Gérard, J.-C., Ritter, B., Hubert, B., Schneider, N. M., & Jain, S. K. (2018). The O(1S) 297.2-nm Dayglow Emission: A Tracer of CO2 Density Variations in the Martian Lower Thermosphere. *Journal of Geophysical Research: Planets*, *123*(12), 3119-3132. doi: 10.1029/2018JE005709

González-Galindo, F., Jiménez-Monferrer, S., López-Valverde, M. Á., García-Comas, M., & Forget, F. (2021, April). On the derivation of thermospheric temperatures from dayglow emissions on Mars. *Icarus*, *358*, 114284. doi: 10.1016/j.icarus.2020.114284

González-Galindo, F., López-Valverde, M. A., Forget, F., García-Comas, M., Millour, E., & Montabone, L. (2015, November). Variability of the Martian thermosphere during eight Martian years as simulated by a ground-to-exosphere global circulation model. *Journal of Geophysical Research (Planets)*, *120*(11), 2020-2035. doi: 10.1002/2015JE004925

Gröller, H., Montmessin, F., Yelle, R. V., Lefèvre, F., Forget, F., Schneider, N. M., ... Jain, S. K. (2018, June). MAVEN/IUVS Stellar Occultation Measurements of Mars Atmospheric Structure and Composition. *Journal of Geophysical Research (Planets)*, *123*(6), 1449-1483. doi: 10.1029/2017JE005466

Gröller, H., Yelle, R. V., Koskinen, T. T., Montmessin, F., Lacombe, G., Schneider, N. M., ... Jakosky, B. M. (2015, November). Probing the Martian atmosphere with MAVEN/IUVS stellar occultations. *Geophysical Research Letters*, *42*(21), 9064-9070. doi: 10.1002/2015GL065294

Gronoff, G., Simon Wedlund, C., Mertens, C. J., Barthélemy, M., Lillis, R. J., & Witasse, O. (2012). Computing uncertainties in ionosphere-airglow models: II. The Martian airglow. *Journal of Geophysical Research: Space Physics*, *117*(A5). doi: 10.1029/2011JA017308

Gupta, N., Venkateswara Rao, N., & Kadhane, U. R. (2019, December). Dawn-Dusk Asymmetries in the Martian Upper Atmosphere. *Journal of Geophysical Research (Planets)*, *124*(12), 3219-3230. doi: 10.1029/2019JE006151

Huestis, D. L., Slanger, T. G., Sharpee, B. D., & Fox, J. L. (2010, Jan). Chemical origins of the Mars ultraviolet dayglow. *Faraday Discussions*, *147*, 307. doi: 10.1039/c003456h

Jain, S. K. (2013). *Dayglow emissions on Mars and Venus* (Doctoral dissertation). Retrieved from `http://dyuthi.cusat.ac.in/purl/3688`

Jain, S. K., Bougher, S. W., Deighan, J., Schneider, N. M., González Galindo, F., Stewart, A. I. F., ... Pawlowski, D. (2020, February). Martian Thermospheric Warming Associated With the Planet Encircling Dust Event of 2018. *Geophysical Research Letters*, *47*(3), e85302. doi: 10.1029/2019GL085302

Jain, S. K., Soto, E., Evans, J., Deighan, J., Schneider, N., & Bougher, S. (2021). Thermal structure of mars' middle and upper atmospheres: Understanding the impacts of dynamics and solar forcing. *Icarus*, 114703. Retrieved from `https://www.sciencedirect.com/science/article/pii/S0019103521003584` doi: https://doi.org/10.1016/j.icarus.2021.114703

Jain, S. K., Stewart, A. I. F., Schneider, N. M., Deighan, J., Stiepen, A., Evans, J. S., ... Jakosky, B. M. (2015, November). The structure and variability of Mars upper atmosphere as seen in MAVEN/IUVS dayglow observations. *Geophysical Research Letters*, *42*(21), 9023-9030. doi: 10.1002/2015GL065419

Keating, G. M., Bougher, S. W., Zurek, R. W., Tolson, R. H., Cancro, G. J., Noll, S. N., ... Babicke, J. M. (1998, March). The Structure of the Upper Atmosphere of Mars: In Situ Accelerometer Measurements from Mars Global Surveyor. *Science*, *279*, 1672. doi: 10.1126/science.279.5357.1672

Kella, D., Vejby-Christensen, L., Johnson, P., Pedersen, H., & Andersen, L. (1997). The source of green light emission determined from a heavy-ion storage ring experiment. *Science*, *276*(5318), 1530–1533.

Krauss, M., & Neumann, D. (1975). On the interaction of o (1s) with o (3p). *Chemical Physics Letters*, *36*(3), 372–374.

Laher, R. R., & Gilmore, F. R. (1990). Updated excitation and ionization cross sections for electron impact on atomic oxygen. *Journal of Physical and Chemical Reference Data*, *19*(1), 277–305.

Leblanc, F., Chaufray, J. Y., Lilensten, J., Witasse, O., & Bertaux, J. L. (2006, August). Martian dayglow as seen by the SPICAM UV spectrograph on Mars Express. *Journal of Geophysical Research (Planets)*, *111*(E9), E09S11. doi: 10.1029/2005JE002664

LeClair, L. R., & McConkey, J. (1993). Selective detection of o (1 s 0) following electron impact dissociation of o2 and n2o using a xeo* conversion technique. *The Journal of chemical physics*, *99*(6), 4566–4577.

Link, R. (1992). Feautrier solution of the electron transport equation. *Journal of Geophysical Research: Space Physics*, *97*(A1), 159–169.

Lo, D. Y., Yelle, R. V., Schneider, N. M., Jain, S. K., Stewart, A. I. F., England, S. L., ... Jakosky, B. M. (2015). Nonmigrating tides in the Martian atmosphere as observed by MAVEN IUVS. *Geophysical Research Letters*, *42*(21), 9057-9063. doi: 10.1002/2015GL066268

Lumpe, J. D., Bevilacqua, R. M., Hoppel, K. W., Krigman, S. S., Kriebel, D. L., Debrestian, D. J., ... Pruvost, P. (1997). POAM II retrieval algorithm and error analysis. *J. Geophys. Res.*, *102*, 23593–23614. doi: 10.1029/97JD00906

Lumpe, J. D., Bevilacqua, R. M., Hoppel, K. W., & Randall, C. E. (2002, November). POAM III retrieval algorithm and error analysis. *Journal of Geophysical Research (Atmospheres)*, *107*, 4575. doi: 10.1029/2002JD002137

Lumpe, J. D., Floyd, L. E., Herring, L. C., Gibson, S. T., & Lewis, B. R. (2007, August). Measurements of thermospheric molecular oxygen from the Solar Ultraviolet Spectral Irradiance Monitor. *Journal of Geophysical Research (Atmospheres)*, *112*, 16308. doi: 10.1029/2006JD008076

Mahaffy, P. R., Benna, M., Elrod, M., Yelle, R. V., Bougher, S. W., Stone, S. W., & Jakosky, B. M. (2015). Structure and composition of the neutral upper atmosphere of mars from the maven ngims investigation. *Geophysical research letters*, *42*(21), 8951–8957.

Majeed, T., & Strickland, D. J. (1997, March). New Survey of Electron Impact Cross Sections for Photoelectron and Auroral Electron Energy Loss Calculations. *Journal of Physical and Chemical Reference Data*, *26*(2), 335-349. doi: 10.1063/1.556008

McCleese, D. J., Schofield, J. T., Taylor, F. W., Abdou, W. A., Aharonson, O., Banfield, D., ... Zurek, R. W. (2008, November). Intense polar temperature inversion in the middle atmosphere on Mars. *Nature Geoscience*, *1*(11), 745-749. doi: 10.1038/ngeo332

McClintock, W. E., Schneider, N. M., Holsclaw, G. M., Clarke, J. T., Hoskins, A. C., Stewart, I., ... Deighan, J. (2015, September). The Imaging Ultraviolet Spectrograph (IUVS) for the MAVEN Mission. *Space Sci. Rev.*, *195*, 75-124. doi: 10.1007/s11214-014-0098-7

Medvedev, A. S., Nakagawa, H., Mockel, C., Yiğit, E., Kuroda, T., Hartogh, P., ... Jakosky, B. M. (2016, April). Comparison of the Martian thermospheric density and temperature from IUVS/MAVEN data and general circulation modeling. *Geophysical Research Letters*, *43*, 3095-3104. doi: 10.1002/2016GL068388

Meier, R., & Picone, J. (1994). Retrieval of absolute thermospheric concentrations from the far uv dayglow: An application of discrete inverse theory. *Journal of Geophysical Research: Space Physics*, *99*(A4), 6307–6320.

Meier, R., Picone, J., Drob, D., Bishop, J., Emmert, J., Lean, J., ... others (2015). Remote sensing of earth's limb by timed/guvi: Retrieval of thermospheric composition and temperature. *Earth and Space Science*, *2*(1), 1–37.

Millour, E., Forget, F., Spiga, A., Vals, M., Zakharov, V., & Montabone, L. (2018). Mars climate database. *From Mars Express to ExoMars*, 68.

Nakagawa, H., Jain, S. K., Schneider, N. M., Montmessin, F., Yelle, R. V., Jiang, F., ... Deighan, J. I. (2020a, February). A Warm Layer in the Nightside Mesosphere of Mars. *Geophysical Research Letters*, *47*(4), e85646. doi: 10.1029/2019GL085646

Nakagawa, H., Terada, N., Jain, S. K., Schneider, N. M., Montmessin, F., Yelle, R. V., ... Jakosky, B. M. (2020b, September). Vertical Propagation of Wave Perturbations in the Middle Atmosphere on Mars by MAVEN/IUVS. *Journal of Geophysical Research (Planets)*, *125*(9), e06481. doi: 10.1029/2020JE006481

Neary, L., Daerden, F., Aoki, S., Whiteway, J., Clancy, R. T., Smith, M., ... Vandaele, A. C. (2020, April). Explanation for the Increase in High-Altitude Water on Mars Observed by NOMAD During the 2018 Global Dust Storm. *Geophysical Research Letters*, *47*(7), e84354. doi: 10.1029/2019GL084354

Peterson, W., Thiemann, E. B., Eparvier, F. G., Andersson, L., Fowler, C., Larson, D., ... others (2016). Photoelectrons and solar ionizing radiation at mars: Predictions versus maven observations. *Journal of Geophysical Research: Space Physics*, *121*(9), 8859–8870.

Picone, J. (2008). Influence of systematic error on least squares retrieval of upper atmospheric parameters from the ultraviolet airglow. *Journal of Geophysical Research: Space Physics*, *113*(A9).

Rodgers, C. D. (2000). *Inverse Methods for Atmospheric Sounding.* WORLD SCIENTIFIC. doi: 10.1142/3171

Shirai, T., Tabata, T., & Tawara, H. (2001). Analytic cross sections for electron collisions with co, co2, and h2o relevant to edge plasma impurities. *Atomic Data and Nuclear Data Tables*, *79*(1), 143–184.

Simon, C., Witasse, O., Leblanc, F., Gronoff, G., & Bertaux, J. L. (2009, Jul). Dayglow on Mars: Kinetic modelling with SPICAM UV limb data. *Planetary and Space Science*, *57*(8-9), 1008-1021. doi: 10.1016/j.pss.2008.08.012

Slanger, T., & Black, G. (1981). Quenching of 0 ('s) by 02 (a'a,). *Geophys. Res. Lett*, *8*, 535.

Snowden, D., Yelle, R., Cui, J., Wahlund, J.-E., Edberg, N., & Ågren, K. (2013). The thermal structure of Titan's upper atmosphere, I: Temperature profiles from Cassini INMS observations. *Icarus*, *226*(1), 552 - 582. doi: https://doi.org/10.1016/j.icarus.2013.06.006

Starichenko, E. D., Belyaev, D. A., Medvedev, A. S., Fedorova, A. A., Korablev, O. I., Trokhimovskiy, A., ... Hartogh, P. (2021). Gravity wave activity in the martian atmosphere at altitudes 20-160 km from acs/tgo occultation measurements. *Earth and Space Science Open Archive*, 20. Retrieved from `https://doi.org/10.1002/essoar.10506561.2` doi: 10.1002/essoar.10506561.2

Steele, L. J., Kleinböhl, A., & Kass, D. M. (2021, May). Observations of Ubiquitous Nighttime Temperature Inversions in Mars' Tropics After Large Scale Dust Storms. *Geophysics Research Letters*, *48*(9), e92651. doi: 10.1029/2021GL092651

Steffl, A. J., Young, L. A., Strobel, D. F., Kammer, J. A., Evans, J. S., Stevens, M. H., ... others (2020). Pluto's ultraviolet spectrum, surface reflectance, and airglow emissions. *The Astronomical Journal*, *159*(6), 274.

Stevens, M. H., Evans, J. S., Lumpe, J., Westlake, J. H., Ajello, J. M., Bradley, E. T., & Esposito, L. W. (2015a, February). Molecular nitrogen and methane density retrievals from Cassini UVIS dayglow observations of Titan's upper atmosphere. *Icarus*, *247*, 301-312. doi: 10.1016/j.icarus.2014.10.008

Stevens, M. H., Evans, J. S., Schneider, N. M., Stewart, A. I. F., Deighan, J., Jain, S. K., ... Jakosky, B. M. (2015b). New observations of molecular nitrogen in

the Martian upper atmosphere by IUVS on MAVEN. *Geophysical Research Letters*, *42*(21), 9050-9056. doi: 10.1002/2015GL065319

Stevens, M. H., Gustin, J., Ajello, J. M., Evans, J. S., Meier, R., Kochenash, A. J., ... others (2011). The production of titan's ultraviolet nitrogen airglow. *Journal of Geophysical Research: Space Physics*, *116*(A5).

Stevens, M. H., Siskind, D. E., Evans, J. S., Jain, S. K., Schneider, N. M., Deighan, J., ... Jakosky, B. M. (2017, May). Martian mesospheric cloud observations by IUVS on MAVEN: Thermal tides coupled to the upper atmosphere. *Geophysical Research Letters*, *44*(10), 4709-4715. doi: 10.1002/2017GL072717

Stewart, A. I., Barth, C. A., Hord, C. W., & Lane, A. L. (1972, October). Mariner 9 Ultraviolet Spectrometer Experiment: Structure of Mars's Upper Atmosphere (A 5. 3). *Icarus*, *17*(2), 469-474. doi: 10.1016/0019-1035(72)90012-7

Stiepen, A., Gérard, J.-C., Bougher, S., Montmessin, F., Hubert, B., & Bertaux, J.-L. (2015). Mars thermospheric scale height: Co cameron and co2+ dayglow observations from mars express. *Icarus*, *245*, 295–305.

Stone, S. W., Yelle, R. V., Benna, M., Elrod, M. K., & Mahaffy, P. R. (2018). Thermal structure of the martian upper atmosphere from maven ngims. *Journal of Geophysical Research: Planets*, *123*(11), 2842–2867.

Stone, S. W., Yelle, R. V., Benna, M., Elrod, M. K., & Mahaffy, P. R. (2022, June). Neutral Composition and Horizontal Variations of the Martian Upper Atmosphere From MAVEN NGIMS. *Journal of Geophysical Research (Planets)*, *127*(6), e07085. doi: 10.1029/2021JE007085

Stone, S. W., Yelle, R. V., Benna, M., Lo, D. Y., Elrod, M. K., & Mahaffy, P. R. (2020). Hydrogen escape from mars is driven by seasonal and dust storm transport of water. *Science*, *370*(6518), 824–831.

Strickland, D., Bishop, J., Evans, J., Majeed, T., Shen, P., Cox, R., ... Huffman, R. (1999). Atmospheric ultraviolet radiance integrated code (auric): Theory, software architecture, inputs, and selected results. *Journal of Quantitative Spectroscopy and Radiative Transfer*, *62*(6), 689–742.

Thaller, S. A., Andersson, L., Pilinski, M. D., Thiemann, E., Withers, P., Elrod, M., ... Jenkins, G. (2020, May). Tidal Wave-Driven Variability in the Mars Ionosphere-Thermosphere System. *Atmosphere*, *11*(5), 521. doi: 10.3390/atmos11050521

Thiemann, E. M. B., Chamberlin, P. C., Eparvier, F. G., Templeman, B., Woods, T. N., Bougher, S. W., & Jakosky, B. M. (2017, March). The MAVEN EUVM model of solar spectral irradiance variability at Mars: Algorithms and results. *Journal of Geophysical Research (Space Physics)*, *122*(3), 2748-2767. doi: 10.1002/2016JA023512

Thiemann, E. M. B., Eparvier, F. G., Bougher, S. W., Dominique, M., Andersson, L., Girazian, Z., ... Jakosky, B. M. (2018, September). Mars Thermospheric Variability Revealed by MAVEN EUVM Solar Occultations: Structure at Aphelion and Perihelion and Response to EUV Forcing. *Journal of Geophysical Research (Planets)*, *123*(9), 2248-2269. doi: 10.1029/2018JE005550

Vandaele, A. C., Korablev, O., Daerden, F., Aoki, S., Thomas, I. R., Altieri, F., ... Zorzano, M. P. (2019, April). Martian dust storm impact on atmospheric H_2O and D/H observed by ExoMars Trace Gas Orbiter. *Nature*, *568*(7753), 521-525. doi: 10.1038/s41586-019-1097-3

Venot, O., Bénilan, Y., Fray, N., Gazeau, M.-C., Lefèvre, F., Es-sebbar, E., ... others (2018). Vuv-absorption cross section of carbon dioxide from 150 to 800 k and applications to warm exoplanetary atmospheres. *Astronomy & Astrophysics*, *609*, A34.

Viggiano, A. A., Ehlerding, A., Hellberg, F., Thomas, R. D., Zhaunerchyk, V., Geppert, W. D., ... Österdahl, F. (2005). Rate constants and branching ratios for the dissociative recombination of co 2+. *The Journal of chemical physics*, *122*(22), 226101.

Withers, P., Bougher, S. W., & Keating, G. M. (2003, July). The effects of topographically-controlled thermal tides in the martian upper atmosphere as seen by the MGS accelerometer. *Icarus*, *164*, 14-32. doi: 10.1016/S0019-1035(03)00135-0

Wolkenberg, P., Giuranna, M., Smith, M. Â. D., Grassi, D., & Amoroso, M. (2020, March). Similarities and Differences of Global Dust Storms in MY 25, 28, and 34. *Journal of Geophysical Research (Planets)*, *125*(3), e06104. doi: 10.1029/2019JE006104

Yiğit, E. (2021). Martian water escape and internal waves. *Science*, *374*(6573), 1323–1324.

Yiğit, E., Medvedev, A. S., & Hartogh, P. (2018, December). Influence of gravity waves on the climatology of high-altitude Martian carbon dioxide ice clouds. *Annales Geophysicae*, *36*(6), 1631-1646. doi: 10.5194/angeo-36-1631-2018

Yiğit, E., Medvedev, A. S., Benna, M., & Jakosky, B. M. (2021, March). Dust Storm Enhanced Gravity Wave Activity in the Martian Thermosphere Observed by MAVEN and Implication for Atmospheric Escape. *Geophysical Research Letters*, *48*(5), e92095. doi: 10.1029/2020GL092095

Zurek, R., Tolson, R., Bougher, S., Lugo, R., Baird, D., Bell, J., & Jakosky, B. (2017). Mars thermosphere as seen in maven accelerometer data. *Journal of Geophysical Research: Space Physics*, *122*(3), 3798–3814.